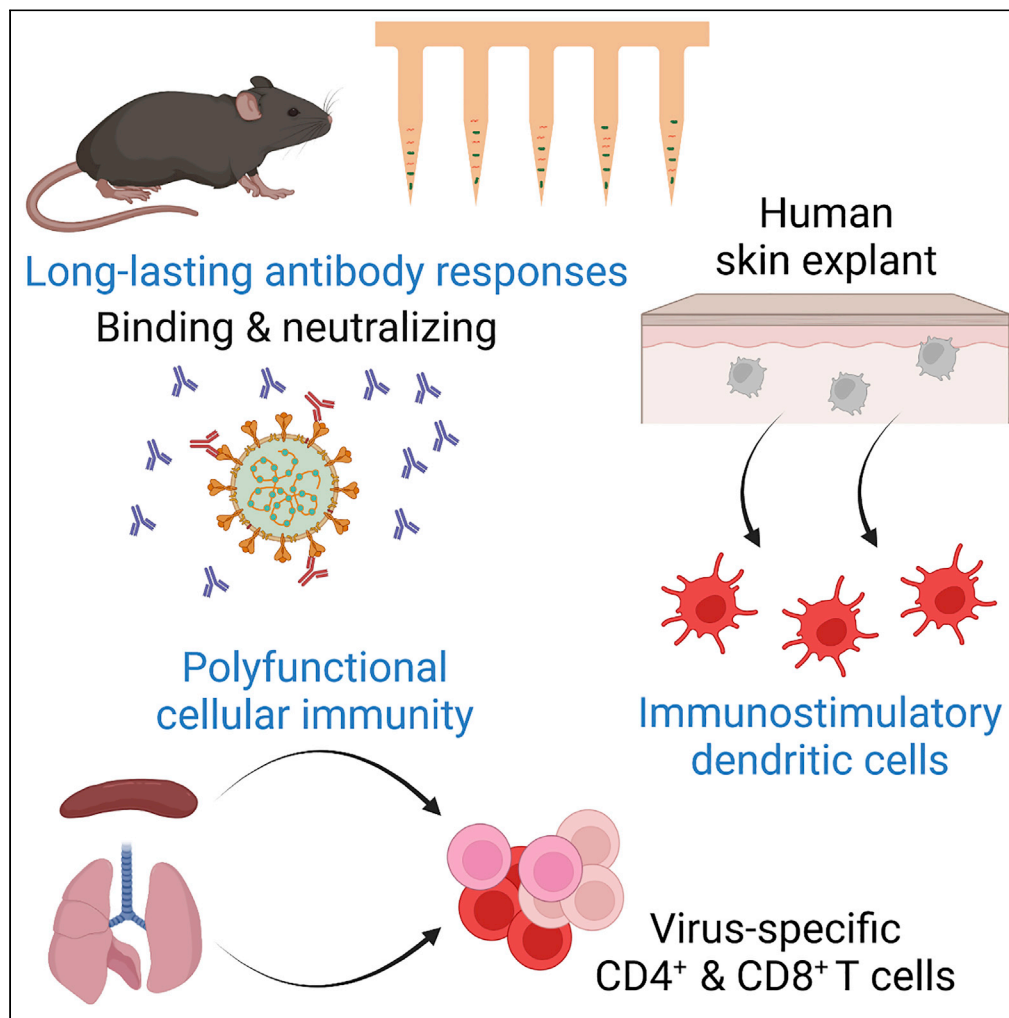


## Article

## A microarray patch SARS-CoV-2 vaccine induces sustained antibody responses and polyfunctional cellular immunity



Stephen C. Balmert, Zohreh Gholizadeh Ghouloujeh, Cara Donahue Carey, ..., Geza Erdos, Emrullah Korkmaz, Louis D. Faló, Jr.

ek001@pitt.edu (E.K.)  
lof2@pitt.edu (L.D.F.)

**Highlights**

An immunogenic, safe, shelf-stable microarray patch (MAP) SARS-CoV-2 vaccine

Polyfunctional cellular immunity and long-lasting antibody responses

Robust respiratory tract immunity via skin vaccination

Translational immune correlates of MAP SARS-CoV-2 vaccine in human skin

Balmert et al., iScience 25, 105045  
October 21, 2022 © 2022 The Author(s).  
<https://doi.org/10.1016/j.isci.2022.105045>

## Article

## A microarray patch SARS-CoV-2 vaccine induces sustained antibody responses and polyfunctional cellular immunity

Stephen C. Balmert,<sup>1</sup> Zohreh Gholizadeh Ghouloujeh,<sup>1</sup> Cara Donahue Carey,<sup>1</sup> Li'an H. Williams,<sup>1</sup> Jiyong Zhang,<sup>1</sup> Preeti Shahi,<sup>1</sup> Maher Amer,<sup>1</sup> Tina L. Sumpter,<sup>1,2</sup> Geza Erdos,<sup>1</sup> Emrullah Korkmaz,<sup>1,3,\*</sup> and Louis D. Faló,<sup>1,3,4,5,6,7,\*</sup>

## SUMMARY

**Sustainable global immunization campaigns against COVID-19 and other emerging infectious diseases require effective, broadly deployable vaccines. Here, we report a dissolvable microarray patch (MAP) SARS-CoV-2 vaccine that targets the immunoresponsive skin microenvironment, enabling efficacious needle-free immunization. Multicomponent MAPs delivering both SARS-CoV-2 S1 subunit antigen and the TLR3 agonist Poly(I:C) induce robust antibody and cellular immune responses systemically and in the respiratory mucosa. MAP vaccine-induced antibodies bind S1 and the SARS-CoV-2 receptor-binding domain, efficiently neutralize the virus, and persist at high levels for more than a year. The MAP platform reduces systemic toxicity of the delivered adjuvant and maintains vaccine stability without refrigeration. When applied to human skin, MAP vaccines activate skin-derived migratory antigen-presenting cells, supporting the feasibility of human translation. Ultimately, this shelf-stable MAP vaccine improves immunogenicity and safety compared to traditional intramuscular vaccines and offers an attractive alternative for global immunization efforts against a range of infectious pathogens.**

## INTRODUCTION

Severe acute respiratory syndrome coronavirus 2 (SARS-CoV-2), the causative agent of the coronavirus disease 2019 (COVID-19) pandemic, is a reminder of unparalleled challenges posed by emerging and re-emerging infectious pathogens (Fauci et al., 2020; Morens and Fauci, 2020). Safe, effective, and broadly deployable vaccines are essential to defend against COVID-19 and future pandemics (Fontanet et al., 2021; Frederiksen et al., 2020). Indeed, striking progress has been made in developing SARS-CoV-2 vaccines since the emergence of COVID-19 (Chung et al., 2020; Connors et al., 2021). However, the efficacy of prevailing SARS-CoV-2 vaccine candidates appears to decline within months (Callaway, 2021; Feikin et al., 2022), and these vaccine platforms impose several limitations for mass vaccination, including logistical, economic, and safety concerns that contribute to vaccine hesitancy (Giudice and Campbell, 2006; Kersten and Hirschberg, 2007; Korkmaz et al., 2021b).

This study presents a dissolvable microarray patch (MAP)-based SARS-CoV-2 vaccine that consists of several sharp-tipped microscopic protrusions that painlessly and transiently breach the superficial skin layers and then dissolve to deliver vaccine components to immune-responsive cutaneous microenvironments. The MAP vaccination platform offers advantages in immunogenicity, safety, distribution, and compliance compared to existing vaccination platforms (Korkmaz et al., 2021a; Suh et al., 2014). Compared to immunization via intramuscular or subcutaneous injections, MAP vaccination can improve antigen-specific immune responses qualitatively and quantitatively (Gill et al., 2014; Sullivan et al., 2010). A growing body of evidence from pre-clinical studies demonstrates that MAPs can deliver vaccine components into specific immune-responsive cutaneous layers precisely and reproducibly (Marshall et al., 2016; Nguyen et al., 2020; Sullivan et al., 2010; Vrdoljak, 2013). Furthermore, skin immunization can induce broad mucosal responses, providing advantages over parenteral immunizations for protection against respiratory pathogens (Liu et al., 2010). This is supported by a recent study that has shown that skin vaccination using

<sup>1</sup>Department of Dermatology, University of Pittsburgh School of Medicine, Pittsburgh, PA 15213, USA

<sup>2</sup>Department of Immunology, University of Pittsburgh School of Medicine, Pittsburgh, PA 15261, USA

<sup>3</sup>Department of Bioengineering, University of Pittsburgh Swanson School of Engineering, Pittsburgh, PA 15261, USA

<sup>4</sup>UPMC Hillman Cancer Center, Pittsburgh, PA 15232, USA

<sup>5</sup>Clinical and Translational Science Institute, University of Pittsburgh, Pittsburgh, PA 15213, USA

<sup>6</sup>The McGowan Institute for Regenerative Medicine, University of Pittsburgh, Pittsburgh, PA 15219, USA

<sup>7</sup>Lead contact

\*Correspondence: ek001@pitt.edu (E.K.), lof2@pitt.edu (L.D.F.)

<https://doi.org/10.1016/j.isci.2022.105045>



Modified Vaccinia Ankara viral vectors results in potent immune responses in the respiratory mucosa (Pan et al., 2021). Importantly, promising early phase clinical trials with influenza vaccines indicate that dissolvable MAPs can deliver vaccines to humans in a safe and immunogenic manner, as well as provide a more patient-friendly vaccination strategy compared to immunization with sharps, thereby supporting more advanced human studies with MAP vaccines (Hirobe et al., 2015; Rouphael et al., 2017).

MAP vaccination has potential safety and compliance advantages compared to traditional hypodermic needle injection. Hypodermic needle injection requires trained personnel for safe and reliable administration. Moreover, hypodermic needles can cause pain and trypanophobia, and carry inherent risks of improper administration, needlestick injuries, and disease transmission. They are also associated with adverse events, which can result from systemic exposure to injected vaccine components, an important consideration for adjuvant delivery using traditional needle injection. On the other hand, MAPs can be simply and painlessly self-administered, eliminating unsafe injection practices and needle phobia, and reducing the need for medical expertise (Arya and Prausnitz, 2016; Prausnitz, 2017). Furthermore, MAP delivery of high concentrations of vaccine components specifically to the local cutaneous microenvironment both improves immunogenicity and minimizes systemic exposures, further improving safety. Together, these platform features can reduce vaccine hesitancy and increase vaccine compliance.

Traditional vaccines, including current leading SARS-CoV-2 antigen platforms, need continuous refrigeration from production to injection to preserve bioactivity, which accounts for a high percentage of the cost of immunization and creates significant hurdles, especially in resource-limited settings (Chen et al., 2011; Shin et al., 2020). Dissolvable MAP-based vaccines are typically stabilized within a rationally formulated water-soluble biomaterial matrix and can be distributed without an expensive cold chain, thereby enabling simpler and less expensive vaccine distribution and storage, especially in developing countries (Arya and Prausnitz, 2016). As such, global immunization efforts for COVID-19 and emerging SARS-CoV-2 variants would benefit from simpler, shelf-stable vaccine delivery technologies that can reduce the economic and logistical barriers to distribution and storage.

With the aforementioned advantages, MAPs are rapidly emerging to disrupt the established paradigm of hypodermic injections for vaccine delivery (Al-Zahrani et al., 2012; McCrudden et al., 2015; Vrdoljak, 2013). In this study, we present a simple and broadly deployable COVID-19 vaccination strategy using dissolvable MAPs integrating SARS-CoV-2 S1 subunit protein, with or without polyinosinic acid:polycytidylic acid (Poly(I:C)), a Toll-like receptor 3 (TLR3) agonist with potent pro-inflammatory effects in the skin microenvironment. The spike (S) protein of SARS-CoV-2, which consists of S1 and S2 subunits, mediates viral entry into host cells during infection and is considered a rational vaccine target against COVID-19 (Duan et al., 2020; Sternberg and Naujokat, 2020). In addition to emerging studies demonstrating the immunogenicity of the S protein, including full length, S1 subunit, and receptor-binding domain (RBD) variants, we have recently shown that a SARS-CoV-2 S1 subunit MAP vaccine can rapidly and effectively trigger the immune system to produce antigen-specific antibody responses in mice (Kim et al., 2020). Here, we evaluate antibody and cellular immune responses induced by COVID-19 vaccination with multicomponent MAPs and compare them to those elicited by immunization via traditional intramuscular injection. We demonstrate that MAP delivery targets vaccine components to the immune-responsive cutaneous microenvironment in both murine and human skin, enabling activation of the skin immune networks through highly localized antigen and adjuvant delivery. Vaccination of mice with MAPs resulted in robust systemic and respiratory antibody responses, as well as polyfunctional cellular immunity in both the spleen and lungs. MAP co-delivery of Poly(I:C) and S1 improved the magnitude and breadth of antigen-specific cellular immune responses. MAP vaccines induced antibody responses against S1 and the RBD, and efficiently neutralized the virus. Importantly, MAP vaccination resulted in antibody responses that persisted at high levels for at least 18 months, consistent with long-lasting immunity. Compared to traditional intramuscular immunization, MAP immunization demonstrated significant advantages in the induction of IgG2c titers (Th1), neutralization, the persistence of antibody responses, and the induction of CD4<sup>+</sup> and CD8<sup>+</sup> T cell responses in the spleen and respiratory mucosa.

Importantly, unlike IM delivery, MAP delivery of Poly(I:C) did not increase inflammatory cytokines in the serum, a finding consistent with reduced systemic reactogenicity. Furthermore, these MAP-embedded vaccines remained effective after storage for at least a month without refrigeration. Finally, in translational studies, MAP delivery of antigen and Poly(I:C) to human skin increased the immunostimulatory capacity of migratory skin-derived dendritic cells (DCs), as determined by increases in the expression of co-stimulatory

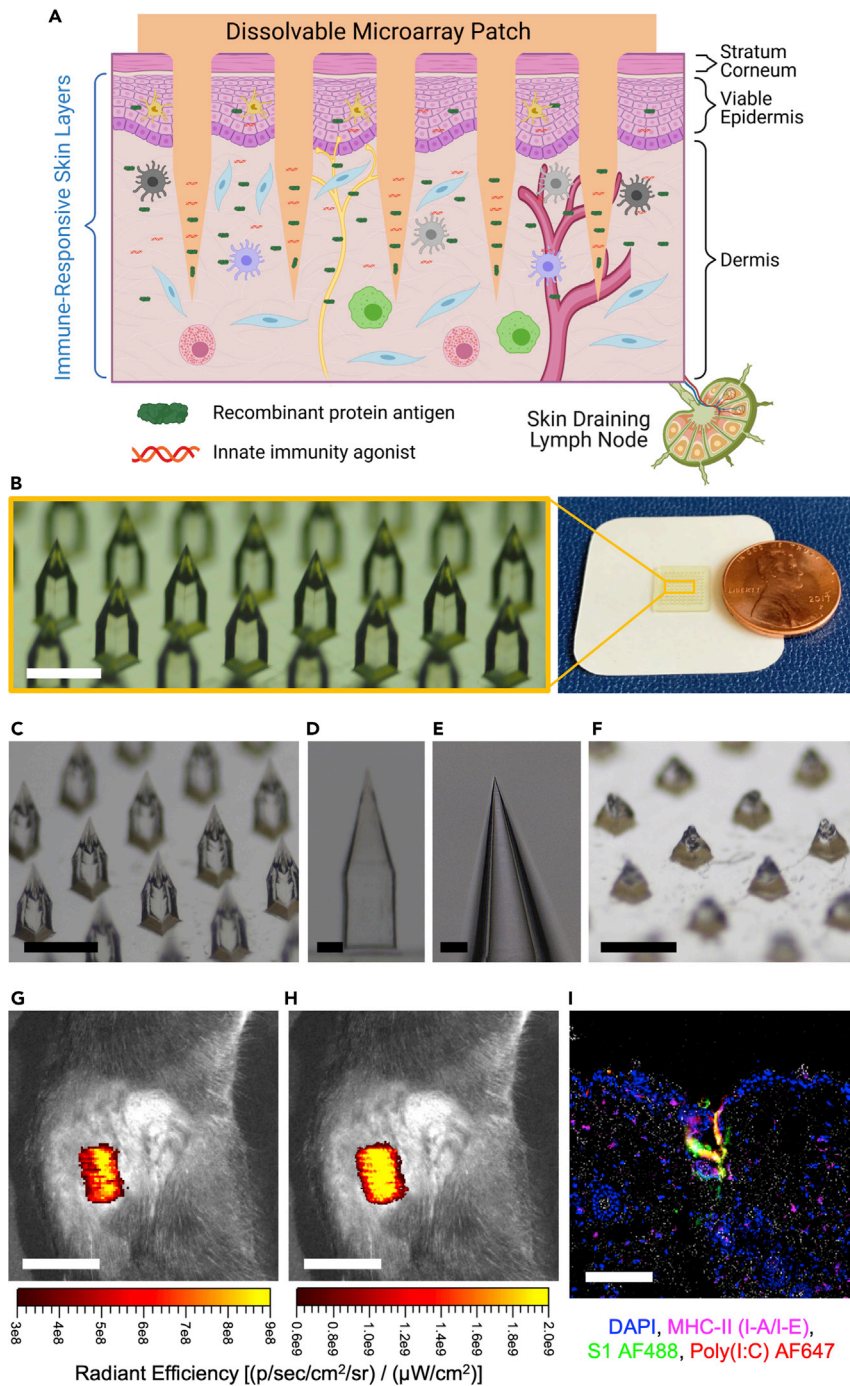


**Figure 1. In situ engineering the cutaneous microenvironment with dissolvable MAPs that deliver multicomponent COVID-19 vaccines**

(A) Intracutaneous vaccination with MAPs harnesses the highly efficient immune circuitry in the skin by precise delivery of antigen and adjuvant.

(B) Images of master MAPs. Scale bar is 500 μm.

(C–E) Optical stereomicroscopy images of obelisk-shaped CMC MAPs. Scale bars in (C), (D), and (E) are 500, 100, and 25 μm, respectively.

(F) Optical stereomicroscopy image of a CMC MAP after application. Scale bar is 500 μm.

(G and H) Effective co-delivery of (G) S1 AF488 and (H) Poly(I:C) AF647 to mouse skin *in vivo* with MAPs, captured using a fluorescence *in vivo* imaging system (IVIS). Scale bars are 10 mm.

**Figure 1. Continued**

(I) Immunofluorescence image with bright-field overlay (gray) shows co-delivery of S1 AF488 (green) and Poly(I:C) AF647 (red) via MAP to the murine abdominal skin microenvironment, replete with MHC-II<sup>+</sup> APCs (magenta). Nuclei were stained with DAPI (blue). Scale bar is 100  $\mu$ m. Separate fluorescence channels and bright-field images are presented in Figure S2.

markers, indicating efficacious *in situ* immune-engineering of the human skin microenvironment. Collectively, our results suggest that MAP delivery is a safe and promising strategy for COVID-19 immunization, and expansion of MAP-based vaccine efforts could enable simple vaccination methods for mass utilization, with increased effectiveness and acceptability. In addition to a rapidly growing body of supporting data from other MAP vaccines, our results encourage further clinical development of MAP-based vaccines for SARS-CoV-2 and other emerging pathogens.

**RESULTS**

**Dissolvable microarray patches for skin-targeted COVID-19 vaccine delivery**

We have exploited our experience with dissolvable MAPs to engineer needle-free, easy-to-apply, patient-friendly, and multifunctional vaccines by formulating recombinant SARS-CoV-2 S1 as an antigen, a TLR3 ligand, Poly(I:C), as an adjuvant, and a water-soluble biomaterial, carboxymethylcellulose (CMC), as a structural material into dissolvable MAPs to harness the cutaneous immune circuitry for simple and painless COVID-19 immunization. MAP vaccination exploits the rich population of professional antigen-presenting cells (APCs) and immunologically active accessory cells within the skin microenvironment, and their highly efficient communication with skin draining lymph nodes, to induce pathogen-specific adaptive immune responses (Figure 1A). Using 3D printed high-quality master MAPs that include a 10  $\times$  10 array of obelisk-shaped, micron-scale protrusions (Figure 1B), our reproducible fabrication strategy, in strict compliance with standard operating procedures for clinical manufacturing, resulted in high-integrity vaccine-loaded dissolvable microprojections with smooth edges and sharp tips (Figures 1C–E). Images of the fabricated CMC MAPs demonstrate high-quality obelisk-shaped micron-scale projections consistent with reliable and reproducible skin penetration and delivery. We evaluated the dissolution of MAPs after *in vivo* application to murine skin for 5, 10, or 15 min using scanning electron microscopy (SEM). As the height of residual undissolved microprojections decreased noticeably from 5 to 15 min (Figure S1), a 15-min application time was used for subsequent experiments in mice. Optical stereomicroscopy images of MAPs after application to skin (Figure 1F) further indicates that these MAPs integrate a design and biomaterial with physicochemical properties required for effective skin penetration and subsequent dissolution. This is in agreement with previous studies that have also shown that CMC is a viable structural material for dissolvable MAPs and provides sufficient mechanical strength for failure-free skin penetration of microprojections (Kim et al., 2013; Shah et al., 2022).

Vaccine components incorporated in MAPs were quantified by S1-specific ELISA and SYBR green assay, which demonstrated reproducible loading of  $21.6 \pm 3.9 \mu\text{g}$  S1 and  $97.3 \pm 3.2 \mu\text{g}$  Poly(I:C) per MAP (mean  $\pm$  SD, N = 6), consistent with the expected loading of 20  $\mu\text{g}$  S1 and 100  $\mu\text{g}$  Poly(I:C) per MAP. To evaluate dissolvable MAP-directed SARS-CoV-2 vaccine delivery to the antigen-presenting cell (APC)-rich cutaneous microenvironments, we next manufactured CMC MAPs integrating Alexa Fluor 488-labeled SARS-CoV-2 S1 antigen and Alexa Fluor 647-labeled Poly(I:C), and applied these S1 AF488 + Poly(I:C) AF647 MAPs to the skin of mice for 15 min. Investigation of MAP-directed skin-targeted delivery of S1 AF488 + Poly(I:C) AF647 in mice using both live animal fluorescence imaging (IVIS) and epifluorescence microscopy of sectioned tissue demonstrates that these MAPs precisely deposit multicomponent COVID-19 vaccine into targeted skin microenvironments that harbor a rich population of MHC class II positive APCs (Figures 1G–1I and S2). S1 MAPs delivered  $77.9 \pm 5.9\%$  of S1 to the skin, whereas S1 + Poly(I:C) MAPs delivered  $75.5 \pm 8.1\%$  of S1 and  $78.8 \pm 6.9\%$  of Poly(I:C) to the skin (mean  $\pm$  SD, N = 5), as determined by comparing fluorescent cargos in MAPs before and after application. As such, these results demonstrate that MAP immunization affords the precise targeting of SARS-CoV-2 vaccine components to immunocompetent skin microenvironments in mice *in vivo*.

**Systemic antibody responses**

As MAP delivery represents a unique immunization route, we next evaluated the safety and immunogenicity of MAP-administered vaccine candidates. Antigen-specific antibody responses are important correlates of vaccine efficacy. We determined SARS-CoV-2-specific serum antibodies induced by MAP-directed immunization of mice that received two doses of SARS-CoV-2 S1 subunit antigen  $\pm$  Poly(I:C) two weeks apart, by application

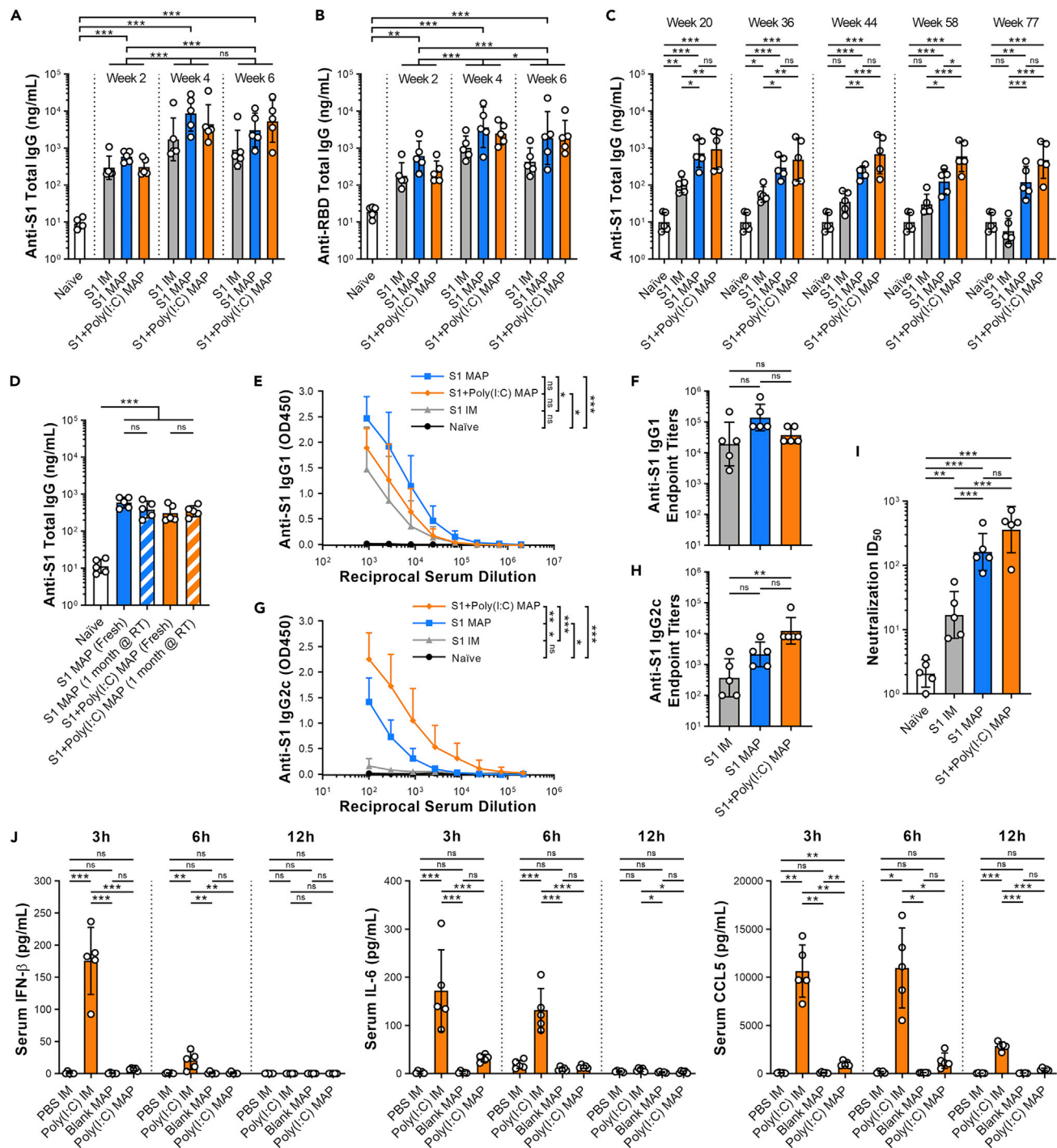


**Figure 2. MAP vaccine-induced antigen-specific antibody responses**

Mice were immunized using SARS-CoV-2 S1 protein (20 μg) ± Poly(I:C) (100 μg) MAPs or by intramuscular (IM) injection of S1 protein (20 μg) on days 0 and 14. (A and B) SARS-CoV-2 (A) S1 binding and (B) RBD binding total IgG concentrations in serum of immunized mice at 2, 4, and 6 weeks after primary immunization. Total IgG concentrations (log<sub>10</sub> transformed) were analyzed by two-way mixed ANOVA, followed by Tukey's test for time effect (non-significant treatment effect). Results were also compared to naive serum by one-way ANOVA, followed by Dunnett's test.

(C) Serum anti-S1 total IgG was also measured 20, 36, 44, 58, and 77 weeks after primary immunization, as in (A). Data (geometric mean ± SD) are from one of two independent experiments, each with N = 5 mice per group. At each time point, serum antibody levels are compared to those from the same five naive samples. (D) Mice were immunized by S1 ± Poly(I:C) MAPs that were freshly prepared as in (A), or stored for 1 month at room temperature after fabrication, and serum anti-S1 total IgG was measured 2 weeks later. Groups in (C-D) were compared by one-way ANOVA on log<sub>10</sub>-transformed data, followed by Tukey's post-hoc tests.

**Figure 2. Continued**

(E) Anti-S1 IgG1 serum titers from mice 6 weeks after primary immunization (mean + SD).

(F) Anti-S1 IgG1 endpoint titers (geometric mean  $\pm$  SD) were calculated from titers in (E).

(G) Anti-S1 IgG2c serum titers from mice 6 weeks after primary immunization (mean + SD).

(H) Anti-S1 IgG2c endpoint titers (geometric mean  $\pm$  SD) calculated from titers in (G). Data are from one of two independent experiments, each with N = 5 mice per group. Titers in (E) and (G) were compared by two-way mixed ANOVA, followed by Holm-Šidák test of treatment effect. Endpoint titers in (F) and (H) were compared by Kruskal-Wallis test, followed by Dunn's multiple comparisons.

(I) SARS-CoV-2-specific neutralizing antibody titers (ID<sub>50</sub>) from mice (geometric mean  $\pm$  SD, N = 5 mice per group) 6 weeks after primary immunization. Groups were compared by one-way ANOVA, followed by Tukey's test.

(J) Intramuscular (IM) injection, but not MAP-mediated delivery, of Poly(I:C) causes a transient, systemic cytokine response. Serum IFN- $\beta$ , IL-6, and CCL5 concentrations in mice 3, 6, and 12 h after administration of 100  $\mu$ g Poly(I:C) via IM injection or MAP were measured by ELISAs. Intramuscular PBS injections and Blank MAPs serve as vehicle controls. Results (mean  $\pm$  SD) are representative from one of two independent experiments, each with N = 5 mice per group. At each time point, groups were compared by one-way ANOVA followed by Tukey's test, or Welch's ANOVA followed by Dunnett's T3 multiple comparisons test. Significant differences are indicated by \*p < 0.05, \*\*p < 0.01 or \*\*\*p < 0.001; ns = not significant (p > 0.05).

of MAPs for 15 min to the right and left sides of the abdomen for prime and boost doses, respectively. We compared antibody responses induced by MAP immunization to those elicited by intramuscular (IM) injections of S1 subunit antigen into hindlimb gastrocnemius muscles also two weeks apart. Naive mice served as unimmunized controls. We measured S1- and RBD-specific total IgG antibody concentrations 2, 4, and 6 weeks after vaccination by ELISA. MAP and IM immunization elicited similarly robust S1- and RBD-specific IgG antibodies as early as 2 weeks after vaccination, and the induced antigen-specific IgG antibodies were enhanced substantially after the boosting dose (Figures 2A and 2B). Importantly, MAP-based immunization induced longer-lasting antibody responses compared to conventional IM vaccination as determined by S1-specific IgG levels at later time points (20, 36, 44, 58, and 77 weeks after immunization). S1-specific antibodies in mice immunized with S1  $\pm$  Poly(I:C) MAPs remained significantly elevated compared to unimmunized controls for at least 18 months, whereas antibody levels in IM immunized mice declined steadily and were no longer significantly elevated compared to unimmunized mice by week 44 (Figure 2C).

To test the stability of COVID-19 vaccine-loaded CMC MAPs, we measured S1-specific total IgG antibody concentrations after vaccination with SARS-CoV-2 S1 (20  $\mu$ g)  $\pm$  Poly(I:C) (100  $\mu$ g) MAPs that had been stored in a sealed amber scintillation vial at room temperature for one month, and compared the resulting antibody responses to those induced by immunization with freshly fabricated MAPs. Results suggest that COVID-19 vaccine-loaded CMC MAPs retained their immunogenicity for at least a month without refrigeration (Figure 2D), indicating temperature stability of our MAP COVID-19 vaccines without dependence on the cold chain.

To evaluate immune skewing of vaccine-induced antibody responses, we determined serum titers of SARS-CoV-2 S1-specific IgG1 and IgG2c six weeks after primary immunization. Mice immunized by MAPs delivering SARS-CoV-2 S1 antigen, with and without Poly(I:C), showed comparable antigen-specific IgG1 titers to mice vaccinated by IM injection of the same antigen (Figures 2E and 2F), suggesting that neither the vaccination route nor the adjuvant status had a significant effect on S1-specific IgG1 titers. In contrast, mice immunized with multicomponent S1 + Poly(I:C) MAPs had higher IgG2c titers than those immunized with S1 alone via MAPs or IM injection (Figures 2G and 2H), demonstrating that immunization by multicomponent MAPs with a rationally selected adjuvant can affect vaccine-induced skewing of antigen-specific immunity. In particular, IgG1 is associated with Th2 immune responses, whereas IgG2c is associated with Th1 immunity and is generally considered more favorable for protection against respiratory pathogens and control of viral infections (Foulds et al., 2006; Hayashi et al., 2018). Collectively, these results suggest that although SARS-CoV-2 S1 subunit vaccines induce comparable S1-specific Th2-associated IgG1 responses when administered via MAP or traditional IM injection, multicomponent S1 + Poly(I:C) MAPs elicit more favorable antibody responses with increased virus-specific, Th1-associated IgG2c responses.

After measuring vaccination-induced antigen-specific binding antibodies, we determined the functional efficacy of these antibodies using a SARS-CoV-2 pseudovirus neutralization assay. We measured neutralizing activities of serum antibodies six weeks after primary immunization. Serum from all immunization groups contained significant neutralizing antibody titers (Figure 2I). Notably, MAP vaccination resulted in significantly higher neutralizing antibody titers compared to IM vaccination (Figure 2I), consistent with improved efficacy of MAP skin immunization compared to traditional immunization strategies.

Induction of pathogen-specific adaptive immune responses without compromising safety is essential for vaccine compliance. Despite substantial research on vaccine adjuvants, potential systemic toxicity or

reactogenicity resulting from systemic exposure associated with administration via traditional routes has made clinical translation of such immune potentiators challenging. Cutaneous vaccination may enable safer administration of adjuvants by limiting their systemic exposure (Korkmaz et al., 2021b). Of the numerous biomarkers identified as indicators of systemic reactogenicity, transiently elevated serum cytokine levels following vaccine delivery are important surrogates of systemic inflammation and undesired symptoms (Burny et al., 2019; McKay et al., 2019; Talaat et al., 2018). For example, systemic toxicity has been attributed to increased serum levels of type I interferons (IFN) following delivery of TLR3 ligands (Cunningham et al., 2007; DeClercq et al., 1972; Hafner et al., 2013). To assess systemic inflammation induced by Poly(I:C) administered via different routes, we measured serum concentrations of several pro-inflammatory, pyrogenic biomarkers (IFN- $\beta$ , IL-6, CCL5, TNF, and IFN- $\gamma$ ) after MAP or intramuscular delivery of Poly(I:C). Although TNF and IFN- $\gamma$  were undetectable, intramuscular injection of Poly(I:C) significantly increased serum levels of IFN- $\beta$ , IL-6, and CCL5 within 3 h of administration, with IFN- $\beta$  and IL-6 levels returning to baseline by 12 h, and CCL5 remaining significantly elevated at 12 h (Figure 2J). Conversely, there were no significant increases in IFN- $\beta$  or IL-6, and only a small increase in CCL5 3 h after cutaneous delivery of Poly(I:C) via MAPs (Figure 2J), suggesting that MAPs may enable localized modulation of immune networks in the skin with reduced systemic adverse effects. Collectively, these results indicate that dissolvable MAPs can efficiently deliver antigens  $\pm$  adjuvants to APC-rich microenvironments within the skin to induce potent antibody immune responses against SARS-CoV-2, and MAP immunization could minimize systemic exposure to adjuvants and prevent potential adverse events.

### Systemic cellular immune responses

Cellular immune responses to SARS-CoV-2 vaccines are important to support antibody responses and can provide direct defense against infection through cytokine release and direct killing of infected cells. Therefore, we evaluated systemic SARS-CoV-2 S1-specific T cell responses in immunized mice 5 days after boosting. Splenocytes from immunized and naive mice were stimulated with a pool of peptides spanning the entire SARS-CoV-2 S1 protein sequence (S1 PepTivator), and then flow cytometry was used to identify S1-specific, cytokine-producing T cells. In particular, we evaluated expression of IFN- $\gamma$ , TNF, IL-2, and IL-4 to identify populations of mono- and polyfunctional T cells, which produce one or more cytokines, respectively, in response to antigen stimulation (Figures 3 and S4). Frequencies of S1-specific IFN- $\gamma$ -producing CD4<sup>+</sup> (Th1) and CD8<sup>+</sup> (Tc1) T cells, as well as CD4<sup>+</sup> IFN- $\gamma$ <sup>-</sup> effector T cells, are presented in Figure 3, and additional subsets, including CD4<sup>+</sup> IL-4<sup>+</sup> Th2, are presented in Figure S4. Intramuscular vaccination caused a slight, but insignificant, increase in S1-specific splenic CD4<sup>+</sup> and CD8<sup>+</sup> T cells, compared to unimmunized naive controls (Figures 3 and S4). Targeting S1 antigen delivery to the skin with MAPs induced significantly greater antigen-specific Tc1 responses, with respect to naive and intramuscular S1 groups (Figure 3E), as well as significantly greater CD4<sup>+</sup> IFN- $\gamma$ <sup>-</sup> effector T cell subsets, compared to naive controls (Figure 3D). However, Th1 responses in the absence of adjuvant were not significant (Figure 3C). In contrast, multicomponent immunization with S1 + Poly (I:C) MAPs significantly enhanced both S1-specific Th1 and CD4<sup>+</sup> IFN- $\gamma$ <sup>-</sup> effector T cell responses (Figures 3C and 3D), compared to all other groups, and induced greater Tc1 responses than S1 MAPs (Figure 3E). Importantly, S1  $\pm$  Poly(I:C) MAPs elicited significant S1-specific polyfunctional Tc1 responses, and significant polyfunctional Th1 and CD4<sup>+</sup> IFN- $\gamma$ <sup>-</sup> effector T cells, including T cells that co-expressed IFN- $\gamma$ , TNF, and IL-2 (Figures 3 and S4). Furthermore, S1  $\pm$  Poly(I:C) MAP immunization did not induce significant S1-specific Th2 populations (Figure S4). To confirm the induction of systemic memory T cell responses, we also measured T cells in mice immunized with S1 + Poly(I:C) MAPs 5 weeks after boosting. While S1-specific T cells underwent a contraction phase resulting in lower frequencies than those observed 5 days post-boost, significant polyfunctional Th1 and Tc1 responses were still detected in spleens of immunized mice (Figures S5A and S5B) 5 weeks post-boost, and these cells were predominantly CD44<sup>+</sup> (Figure S5E), consistent with a memory phenotype.

### Vaccine-induced respiratory tract immunity

Generation of antigen-specific, lung-resident T cells is an important correlate of vaccine efficacy against respiratory viruses (Channappanavar et al., 2014; Zens et al., 2016). Intracutaneous vaccination can induce adaptive immune responses at distant sites, and emerging data suggest that cutaneous delivery of vaccines could be more effective than conventional routes in generating antigen-specific cell-mediated immune responses against respiratory pathogens (Pan et al., 2021). To evaluate cellular immune responses in the lungs of immunized mice, lymphocytes were isolated from the lungs 5 days after boosting, as previously described (Kadoki et al., 2017), and were stimulated with S1 PepTivator. Intracellular cytokine staining and flow cytometry allowed us to identify polyfunctional SARS-CoV-2 S1-specific T cells present in the lungs (Figures 4 and S7). In particular,

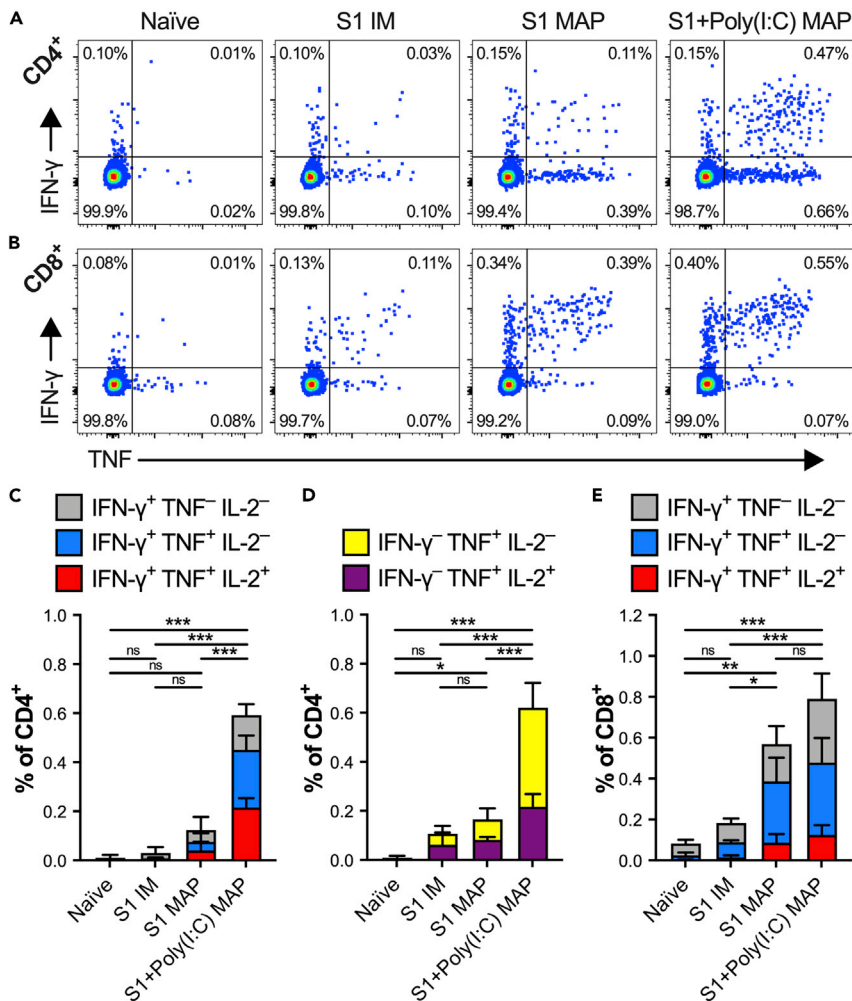


**Figure 3. Systemic antigen-specific T cell responses**

(A–E). Mice were immunized using SARS-CoV-2 S1 protein (20  $\mu$ g)  $\pm$  Poly(I:C) (100  $\mu$ g) MAPs or by intramuscular (IM) injection of S1 protein (20  $\mu$ g) on days 0 and 14, and 5 days later, splenocytes were stimulated with SARS-CoV-2 S1 PepTivator, followed by intracellular cytokine staining and flow cytometry. Representative flow cytometry plots show multifunctional SARS-CoV-2 S1-specific live (A) CD4<sup>+</sup> or (B) CD8<sup>+</sup> T cells expressing IFN- $\gamma$  and/or TNF. The associated gating strategy is presented in Figure S3. Frequencies of SARS-CoV-2 S1-specific live (C) CD4<sup>+</sup> IFN- $\gamma$ <sup>+</sup> TNF<sup>+/–</sup> IL-2<sup>+/–</sup> IL-4<sup>-</sup> T cells (Th1), (D) CD4<sup>+</sup> IFN- $\gamma$ <sup>-</sup> TNF<sup>+</sup> IL-2<sup>+/–</sup> IL-4<sup>-</sup> T cells (IFN- $\gamma$ <sup>-</sup> effector T cells), and (E) CD8<sup>+</sup> IFN- $\gamma$ <sup>+</sup> TNF<sup>+/–</sup> IL-2<sup>+/–</sup> IL-4<sup>-</sup> T cells (Tc1) are shown. Additional T cell subsets are presented in Figure S4. Cytokine positive T cell frequencies are presented after subtracting background responses detected in corresponding unstimulated splenocyte samples, and results (mean  $\pm$  SD) are representative of one of two independent experiments, each with N = 5 mice per group. Groups were compared by one-way ANOVA, followed by Tukey’s test, and significant differences are indicated by \*p < 0.05, \*\*p < 0.01, \*\*\*p < 0.001; ns = not significant (p > 0.05).

the frequency of antigen-specific Th1 (Figure 4C), CD4<sup>+</sup> IFN- $\gamma$ <sup>-</sup> effector T cells (Figure 4D), and Tc1 cells (Figure 4E) in the lungs of immunized mice and naive controls were quantified. Consistent with the minimal systemic S1-specific T cell responses found in spleen; intramuscular immunization failed to elicit significant S1-specific T cell responses in the lungs (Figures 4C–E). Immunization with S1 MAPs generated significant lung Tc1 responses compared to naive or intramuscularly vaccinated mice (Figure 4E). Notably, vaccination with multicomponent S1 + Poly(I:C) MAPs significantly enhanced levels of Th1 (Figure 4C) and CD4<sup>+</sup> IFN- $\gamma$ <sup>-</sup> effector T cell populations (Figure 4D), compared to all other groups, but the inclusion of Poly(I:C) adjuvant did not further enhance the Tc1 response in the lungs, compared to S1 MAPs (Figure 4E). As with systemic T cell responses evaluated in spleens, a large proportion of respiratory tract S1-specific T cells were also polyfunctional, producing two or more Th1/Tc1-associated cytokines (i.e., IFN- $\gamma$ , TNF, and IL-2) (Figures 4 and S7). Collectively, these results

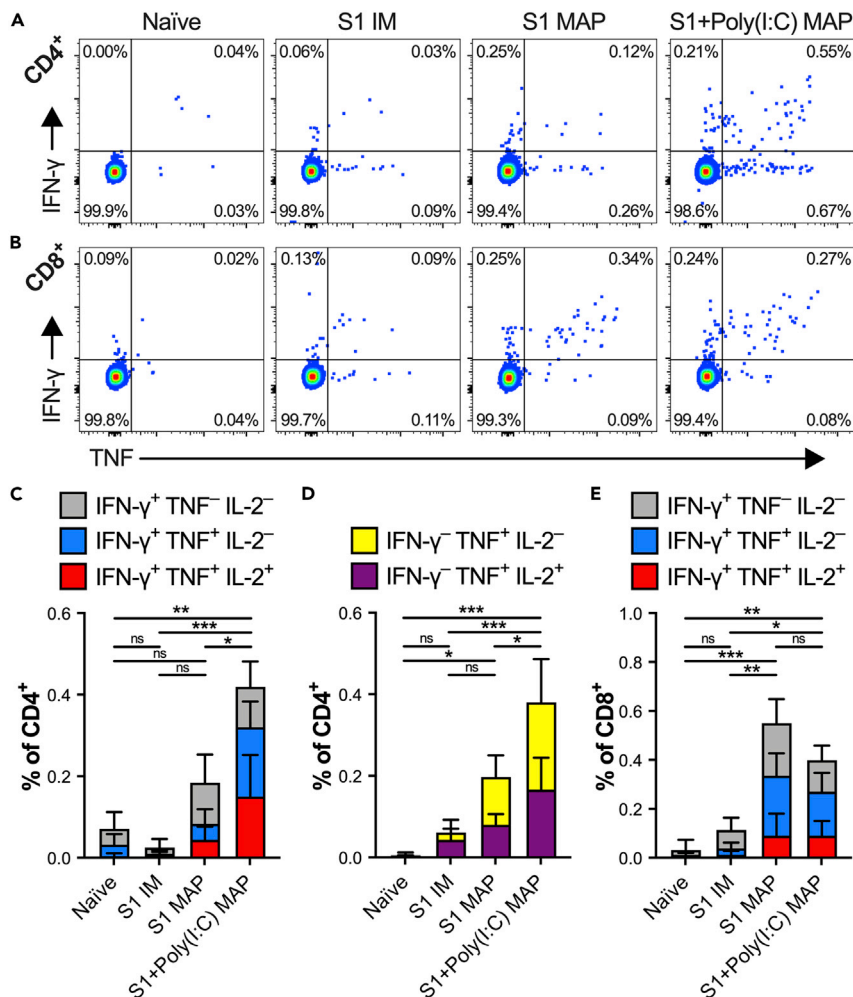


**Figure 4. Antigen-specific T cell responses in lungs**

(A–E). Mice were immunized using SARS-CoV-2 S1 protein (20  $\mu$ g)  $\pm$  Poly(I:C) (100  $\mu$ g) MAPs or by intramuscular (IM) injection of S1 protein (20  $\mu$ g) on days 0 and 14. Five days later, lymphocytes isolated from the lungs of immunized mice and naive controls were stimulated with SARS-CoV-2 S1 PepTivator, followed by intracellular cytokine staining and flow cytometry. Representative flow cytometry plots show multifunctional SARS-CoV-2 S1-specific live (A) CD4<sup>+</sup> or (B) CD8<sup>+</sup> T cells expressing IFN- $\gamma$  and/or TNF. The associated gating strategy is presented in Figure S6. Frequencies of SARS-CoV-2 S1-specific (C) CD4<sup>+</sup> IFN- $\gamma$ <sup>+</sup> TNF<sup>+/−</sup> IL-2<sup>+/−</sup> IL-4<sup>−</sup> T cells (Th1), (D) CD4<sup>+</sup> IFN- $\gamma$ <sup>−</sup> TNF<sup>+/−</sup> IL-2<sup>+/−</sup> IL-4<sup>−</sup> T cells (CD4<sup>+</sup> IFN- $\gamma$ <sup>−</sup> effector T cells), and (E) CD8<sup>+</sup> IFN- $\gamma$ <sup>+</sup> TNF<sup>+/−</sup> IL-2<sup>+/−</sup> IL-4<sup>−</sup> T cells (Tc1). Additional T cell subsets are presented in Figure S7. Cytokine positive T cell frequencies are presented after subtracting background responses detected in corresponding unstimulated controls, and results (mean  $\pm$  SD) are representative from one of two independent experiments, each with N = 5 mice per group. Groups were compared by one-way ANOVA, followed by Tukey’s test, and significant differences are indicated by \*p < 0.05, \*\*p < 0.01, \*\*\*p < 0.001; ns = not significant (p > 0.05).

suggest that SARS-CoV-2 S1 subunit vaccines are more effective at inducing lung-resident, antigen-specific T cell responses when delivered to the skin via MAPs, compared to the traditional intramuscular route of immunization, and the strength and breadth of lung-resident T cell responses can be substantially improved by co-delivery of a rationally selected adjuvant (e.g., Poly(I:C)) together with SARS-CoV-2 S1 antigen in the same MAPs. To evaluate memory T cell responses to S1 + Poly(I:C) MAP immunization, we also measured T cells 5 weeks after boosting. Significant S1-specific polyfunctional Th1 responses were detected in lungs of immunized mice at this later time point, whereas polyfunctional Tc1 responses were slightly elevated relative to naive mice (Figures S5C–S5E). Notably, in addition to generating more effective pulmonary cellular immunity compared to other groups, multicomponent S1 + Poly(I:C) MAPs also induced significant respiratory tract antibody responses, as indicated by elevated S1-specific IgG responses in lung tissue homogenates and bronchoalveolar lavage (BAL) fluid six weeks after primary immunization (Figure S8).

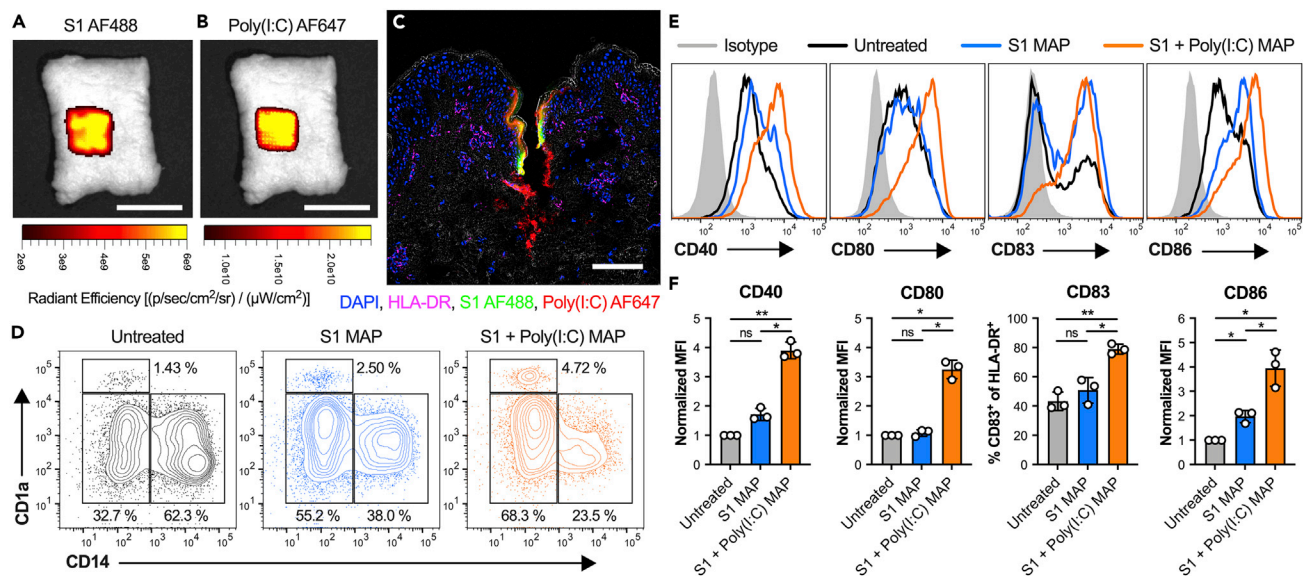


**Figure 5. Dissolvable MAP delivery of a multicomponent SARS-CoV-2 vaccine to human skin**

(A and B). IVIS fluorescence imaging confirms co-delivery of (A) AF488-labeled SARS-CoV-2 S1 and (B) AF647-labeled Poly(I:C) to human skin via MAPs. Images were acquired immediately after application and removal of MAP, and scale bars are 10 mm.

(C) Immunofluorescence image with bright-field overlay (gray) shows co-delivery of S1 AF488 (green) and Poly(I:C) AF647 (red) via MAP to the human skin microenvironment, replete with HLA-DR<sup>+</sup> APCs (magenta). Sections were counterstained with DAPI (blue), and the scale bar is 100  $\mu$ m. Separate fluorescence channels and bright-field images are presented in [Figure S9](#).

(D) Representative flow cytometry plots of total live HLA-DR<sup>+</sup> cells migrating from human skin explants within 48 h of treatment. Gates show frequencies of CD1a<sup>++</sup> LC, CD1a<sup>+</sup> dermal DC, and CD14<sup>+</sup> dermal monocyte-derived DC subsets. The associated gating strategy is presented in [Figure S10](#).

(E) Representative histograms show expression of co-stimulatory receptors on total live HLA-DR<sup>+</sup> cells migrating from human skin explants.

(F) Relative expression of co-stimulatory receptors by total live HLA-DR<sup>+</sup> cells from three independent experiments (different skin donors; mean  $\pm$  SD). Median fluorescence intensity (MFI) values are normalized to those for cells from untreated skin from the same experiment. Because the expression pattern for CD83 is bimodal, percentages of CD83<sup>+</sup> cells are presented instead of normalized MFI. Groups were compared by one-way repeated measures ANOVA with Geisser-Greenhouse correction, followed by Tukey's test. \* $p < 0.05$ , \*\* $p < 0.01$ , ns = not significant.

### MAP delivery of SARS-CoV-2 vaccine to human skin

Human skin explant models offer unique platforms for translational efforts to provide additional support for the clinical efficacy of MAP-delivered vaccines. We performed studies with freshly excised human skin to extend our mechanistic understanding of MAP delivery of SARS-CoV-2 subunit vaccines, with or without an adjuvant. Dissolution of MAPs after application to human skin for 5, 10, or 15 min was evaluated using SEM. Because the size of residual microprojections was comparable at each time point ([Figure S1C](#)), MAPs were applied 5 min in subsequent experiments. To demonstrate delivery of SARS-CoV-2 MAP vaccine components to the immune responsive human skin microenvironment, we fabricated dissolvable MAPs with AF488-labeled S1 protein and AF647-labeled Poly(I:C). After application of S1 AF488 + Poly(I:C) AF647 MAP and subsequent removal of the backing layer, the delivery of fluorescent vaccine components to human skin was confirmed using fluorescence *in vivo* imaging (IVIS) ([Figures 5A](#) and [5B](#)). Dissolving S1 MAPs delivered  $91.7 \pm 1.2\%$  of S1 to the skin, whereas S1 + Poly(I:C) MAPs delivered  $83.9 \pm 4.0\%$  of S1 and  $78.8 \pm 6.9\%$  of Poly(I:C) to the skin (mean  $\pm$  SD,  $N = 4$ ), as determined by comparing fluorescent cargos in MAPs before and after skin applications. Human skin explants treated with S1 AF488 + Poly(I:C) AF647 MAPs were also cryosectioned and skin APCs stained with a fluorescently labeled HLA-DR (MHC class II) antibody. Immunofluorescence microscopy shows co-delivery of labeled S1 and Poly(I:C) to the human skin microenvironment containing abundant HLA-DR<sup>+</sup> APCs ([Figures 5C](#) and [S9](#)).

After demonstrating delivery of vaccine components to human skin with MAPs, we investigated the effects of S1  $\pm$  Poly(I:C) MAPs on the phenotype of APCs migrating from human skin explants within 48 h of application, which represent those that would migrate to skin draining lymph nodes to induce antigen-specific adaptive immune responses. Application of S1 MAPs to human skin led to increased frequencies of CD1a<sup>++</sup> epidermal Langerhans cells (LCs) and CD1a<sup>+</sup> dermal dendritic cells (DCs), and reduced frequencies of CD14<sup>+</sup> monocyte-derived dermal DCs, compared to untreated skin, as determined by flow cytometry

(Figure 5D). Co-delivery of Poly(I:C) with MAPs further enhanced the frequencies of migrating LCs and CD1a<sup>+</sup> dermal DCs and reduced migrating CD14<sup>+</sup> dermal DC populations (Figure 5D). As a surrogate marker of DC stimulatory capacity, we also measured the expression of co-stimulatory surface receptors CD40, CD80, CD83, and CD86 by flow cytometry. Total HLA-DR<sup>+</sup> APCs migrating from human skin after S1 MAP application expressed significantly higher levels of CD86, compared to those from untreated skin (Figures 5E and 5F). Polyfunctional MAPs delivering both S1 and Poly(I:C) induced significantly higher expression of CD40, CD80, CD83, and CD86 by total skin migratory APCs (Figures 5E and 5F), consistent with a more immunostimulatory phenotype (Larregina and Falo, 2005; Mathers and Larregina, 2006; Schmidt et al., 2012). Collectively, these results are consistent with the idea that co-delivery of Poly(I:C) adjuvant via MAPs could enhance human immune responses against SARS-CoV-2 by engineering the human skin microenvironment to induce the T cell activation capacity of antigen-loaded APCs migrating to draining lymph nodes from MAP-immunized sites.

## DISCUSSION

This study was motivated by the historic success of the immunization campaign against smallpox, which used a skin-targeted vaccine, and by recognition of the need for needle-free and temperature-stable vaccine delivery systems to contribute to the fight against COVID-19 and future pandemics. Our main goal was to engineer a shelf-stable, easy-to-administer, dissolvable MAP integrating a SARS-CoV-2 subunit antigen, an innate immune agonist, and a sugar-based, water-soluble biomaterial as a structural component, to enable effective, safe, and broadly deployable COVID-19 vaccines. Subunit vaccines against several pathogens have been used for decades because of their effectiveness, specificity, and established safety profiles (Foged, 2011; Hansson et al., 2000; Moyle and Toth, 2013). We selected recombinant SARS-CoV-2 S1 protein as the antigen for the current studies based on its prior identification as a rational target for vaccines against coronaviruses (Kim et al., 2020; Modjarrad, 2016; Wang et al., 2020, 2021). As a subunit of the spike protein found on the surface of coronaviruses, S1 contains the receptor-binding domain (RBD), which engages receptors on host cells (Benton et al., 2020; Li, 2016). Although subunit vaccines can elicit protective immune responses against targeted viral antigens, they lack the pathogen-associated molecular patterns (PAMPs) present in other types of vaccines, such as those with live attenuated or inactivated viruses, which can stimulate innate immune responses and enhance vaccine immunogenicity. Thus, subunit antigens are often complemented with adjuvants to enhance the strength, breadth, longevity, and quality of induced antigen-specific immune responses (Irvine et al., 2020; O'Hagan and DeGregorio, 2009; Perrie et al., 2008). Accordingly, we engineered multicomponent MAPs to also integrate and co-deliver Poly(I:C), a well-studied TLR3 agonist (Matsumoto and Seya, 2008; Salem et al., 2005). Several factors support the use of Poly(I:C) as a rational adjuvant for skin vaccination to promote enhanced anti-viral immune responses (Borkowski et al., 2013; Tohyama et al., 2005). As a synthetic analog of double-stranded RNA, a PAMP associated with viral infections, Poly(I:C) activates human and murine APCs directly or indirectly (Lebre et al., 2003; Longhi et al., 2009; Oosterhoff et al., 2013; Verdijk et al., 1999). Importantly, Poly(I:C) is particularly potent as a skin adjuvant because TLR3 is expressed by keratinocytes and mediates cell death-induced acute inflammation in the skin (Bernard et al., 2012; Lai et al., 2009; Lai and Gallo, 2008). Moreover, innate inflammation mediated by TLR3 signaling induces secretion of high levels of type I interferons (e.g., IFN- $\beta$ ), which is associated with induction of Th1-skewed CD4<sup>+</sup> T cell responses and CD8<sup>+</sup> T cell responses that protect against pathogens (Hafner et al., 2013; Lai and Gallo, 2008; Lebre et al., 2003; Longhi et al., 2009; Salem et al., 2005). Previous studies also have shown that free Poly(I:C) can be taken up by cells through several mechanisms (Mian et al., 2013; Watanabe et al., 2011), and intracutaneous delivery of free Poly(I:C) is capable of inducing a pro-inflammatory skin phenotype (Bardel et al., 2016; Erdos et al., 2020; Oosterhoff et al., 2013). Importantly, intradermal injection of Poly(I:C) has been shown to cause no overt skin reactogenicity (Bardel et al., 2016), which is consistent with our observation of no visible reactogenicity at MAP vaccine application sites. For the structural material for the SARS-CoV-2 MAP vaccine, we chose CMC because it is considered a "generally recognized as safe" (GRAS) material by the Food and Drug Administration (FDA), and is water-soluble, mechanically strong, moldable, and inexpensive (Balmert et al., 2020). Furthermore, we have used CMC MAPs in ongoing phase I clinical trials (ClinicalTrials.gov Identifiers: NCT02192021 and NCT03646188). In the present study, we exploited two-photon polymerization (2PP)-based three-dimensional (3D) laser lithography, or 3D printing, and room temperature and organic solvent-free micromolding processes to enable manufacturing of high-quality, sharp, obelisk-shaped microprojections incorporating COVID-19 vaccine components. Our results indicate that the MAP-embedded COVID-19 vaccine was resistant to mechanical and thermal stresses, enabling reliable skin penetration without breakage and long-term stability without the need for refrigeration. By reducing the necessary cold chain burden and packaging size, as well

as the need for medical expertise for proper administration, MAP-based vaccination is expected to be more cost-effective than conventional immunization via hypodermic injections.

To establish the MAP platform and actualize the practical and logistical potential of MAPs for needle- and refrigeration-free global immunization campaigns against COVID-19, or other novel pathogens, it is important to establish that MAP immunization is at least as effective as traditional vaccination with hypodermic needles and syringes in terms of inducing pathogen-specific antibody and cellular immune responses. We compared MAP immunization to that with traditional intramuscular injections, hypothesizing that the skin is an ideal target for vaccination because of a high density of skin-resident APCs and innate immune cells, as well as efficient communication of these cells with the skin draining lymph nodes to generate potent and robust adaptive immune responses to vaccines delivered to the cutaneous microenvironment (Korkmaz et al., 2021a, 2021b). This is an important mechanistic advantage over conventional immunization routes, which may be sub-optimal in terms of antigen presentation and immune induction due to the substantially lower density of APCs and relatively immunologically inert characteristics of muscle and subcutaneous tissues (Korkmaz et al., 2021b). MAPs delivered vaccine components to skin immune cells in both mouse and human skin, and intracutaneous immunization with S1 MAPs elicited robust systemic antibody and polyfunctional T cell responses. Both MAP and intramuscular injection routes of antigen administration elicited S1-specific antibody responses, the majority of which bind to the receptor-binding domain (RBD), but S1 MAPs induced longer lasting IgG responses, better neutralization activity, and stronger polyfunctional systemic CD8<sup>+</sup> T cell responses.

Multicomponent S1 + Poly(I:C) MAP immunization further improved the magnitude and breadth of SARS-CoV-2-specific immunity, significantly enhancing IgG2c and polyfunctional Th1 responses, which are important for the clearance of viruses (Martins et al., 2016; Wørzner et al., 2020). Notably, MAP-delivered Poly(I:C) enhanced S1-specific immune responses without significantly increasing serum IFN- $\beta$  and IL-6, which have been associated with systemic toxicity in prior studies (Buglione-Corbett et al., 2013; Cunningham et al., 2007; DeClercq et al., 1972; Hafner et al., 2013; McKay et al., 2019; Wang et al., 2014). Serum CCL5, a pyrogenic chemokine and potent inducer of febrile responses (McKay et al., 2019), was also only minimally elevated at 3 h by Poly(I:C) delivered via MAPs. Interestingly, we previously demonstrated that MAP-delivered Poly(I:C) transiently induces IFN- $\beta$  in the skin at the MAP application site (Erdos et al., 2020), likely contributing to the enhanced immune responses. By delivering adjuvants to the skin and inducing localized innate immune responses, multicomponent MAPs maintain the immunogenicity advantages of adjuvants while reducing the risk of systemic adjuvant toxicity and associated adverse events, or reactogenicity compared to the intramuscular route. Furthermore, CMC has been previously shown to have no significant cytotoxic effect on murine or human skin cells (Yalcintas et al., 2020). Despite these promising results, thorough assessment of the safety of S1 + Poly(I:C) CMC MAPs in human subjects will still be needed to fully understand the effect of each component on local skin health and overall health.

Because SARS-CoV-2 is a respiratory virus, we also evaluated MAP vaccine-induced cellular immunity in the lungs after MAP or intramuscular vaccination. Emerging evidence regarding the skin-lung axis suggests that delivery of antigens to the skin can induce antigen-specific cellular immune responses in the lungs (Pan et al., 2021; Zaric et al., 2019), and immunization via the cutaneous route may be more effective for the generation of protective T cell responses against respiratory pathogens (Pan et al., 2021). In the present study, although intramuscular S1 subunit immunization failed to generate robust T cell responses in the lungs, targeting SARS-CoV-2 vaccine components to the skin microenvironment via MAPs generated significant S1-specific, polyfunctional CD8<sup>+</sup> T cell populations in the lungs. Vaccination with multicomponent S1 + Poly(I:C) MAPs significantly enhanced polyfunctional lung Th1 and CD4<sup>+</sup> TNF<sup>+</sup> effector T cell populations with minimal Th2 responses, indicating the potential for more effective anti-viral immunity, while alleviating concerns of pulmonary Th2 immunopathology (Park et al., 2018). Although the exact mechanisms of the induction of antigen-specific respiratory tract immunity via MAP-based cutaneous vaccination is not fully understood, considerable evidence suggests that engineering the skin microenvironment can generate lymphocytes with distinct tissue homing receptors (Dioszeghy et al., 2017; Zaric et al., 2019). Furthermore, understanding of lymphocyte trafficking mechanisms may enable improved MAP-based skin vaccination strategies with novel adjuvants for tissue-targeted protection against respiratory viruses.

Translational studies with human skin models provide an effective means to validate murine studies. We and several others have previously utilized living human skin explant models for immunological studies (Bandyopadhyay et al., 2022; Boks et al., 2015; Larregina et al., 2001; Morelli et al., 2005; Oosterhoff et al., 2013; Schneider

et al., 2012). Multicomponent MAPs successfully delivered SARS-CoV-2 S1 antigen and Poly(I:C) adjuvant to APC-rich human skin, effectively engineering the skin microenvironment to induce efficient migration of APCs with potent immunostimulatory phenotypes, as evidenced by increased expression of co-stimulatory receptors. In experiments with human skin explant models, normalizing results to untreated controls from each tissue donor can reduce the influence of inherent variability in baseline responses among donors, thereby enabling treatment effects to be identified more consistently in skin samples from multiple donors. In the future, human skin platforms may be useful to evaluate cutaneous immune responses to other MAP-delivered vaccines comprising different antigen formats (e.g., subunit, inactivated virus, viral vector, or mRNA), antigenic targets (e.g., spike proteins or other viral structural proteins), and/or adjuvants.

With a global commitment to the COVID-19 pandemic response, there is an opportunity to build on this momentum to develop more effective vaccination strategies against SARS-CoV-2 and other emerging pathogens. Together with emerging evidence from studies with MAP vaccines against SARS-CoV-2 (Kim et al., 2020; Kuwentrai et al., 2021; McMillan et al., 2021, 2022; Xia et al., 2021) and other viruses (Korkmaz et al., 2021b; Marshall et al., 2016; Nguyen et al., 2020; Rodgers et al., 2019), our results suggest that this MAP-based vaccination platform could enable simple, cost-effective global immunization campaigns against SARS-CoV-2 and other emerging infectious pathogens, with improved immunogenicity, safety, distribution, and compliance that together would improve coverage compared to vaccination using hypodermic needles and syringes. Our study comprehensively evaluated long-term antibody responses and polyfunctional cellular immune responses (both systemic and in the respiratory tract) to a MAP-based SARS-CoV-2 S1 subunit vaccine, with or without the Th1-skewing adjuvant Poly(I:C). Moreover, our results demonstrate the translational potential of S1 ± Poly(I:C) MAPs using living human skin models. Thus, these results significantly add to the rapidly growing body of evidence supporting the development of MAP vaccines against infectious diseases. In addition, MAP subunit vaccines may enable simplified seasonal vaccination programs to boost immunity and provide protection against newly identified SARS-CoV-2 variants. They could also be a preferred vaccine platform to boost individuals previously vaccinated with viral vector-based (e.g., adenovirus) SARS-CoV-2 vaccines because vector-specific immune responses can reduce the effectiveness of subsequent immunization with the same vector (Chmielewska et al., 2014; Jung et al., 2018).

In summary, we have engineered an immunogenic, safe, room temperature stable, and cost-effective multicomponent MAP vaccine platform, comprising SARS-CoV-2 S1 subunit antigen, Poly(I:C), and biocompatible CMC hydrogel, to enable simple, needle-free, painless, and potentially self-administrated immunization to improve vaccine efficacy, logistics, and compliance. Compared to vaccination via the traditional intramuscular route, MAP immunization elicited broader and stronger virus-specific antibody and cellular immunity, with further enhancement of Th1-type responses induced by the inclusion of Poly(I:C). This needle-free vaccine targets antigen and adjuvant to the immunologically rich cutaneous microenvironment in a simple, painless, and efficient manner, increasing immunogenicity while improving safety by reducing systemic exposure to vaccine components. MAPs maintain vaccine stability without the need for refrigeration, and dissolve in the skin, eliminating unsafe sharps waste. Dissolvable MAPs are shelf-stable, self-administered, and versatile skin-targeted vaccine delivery systems that can be formulated to integrate various antigen platforms and adjuvants for vaccination against SARS-CoV-2, or other infectious pathogens. They can also readily be stockpiled for distribution to support future global vaccination campaigns. As such, the MAP platform offers mechanistic and practical advantages over traditional intramuscular immunization with needles and syringes. Collectively, our results support the emerging notion that MAPs have significant potential to disrupt the current established vaccine paradigm, and encourage further development and translation of MAP-based vaccines to combat COVID-19 and contribute to future pandemic preparedness.

### Limitations of the study

This study details the promising immunogenicity of a MAP-based SARS-CoV-2 vaccine as defined by antigen-specific humoral and cellular immune responses, including the induction of these immune responses in the respiratory mucosa. Future studies will be needed to confirm the ability of COVID-19 MAP vaccines, with or without strategically selected adjuvants, to protect against SARS-CoV-2 infection in murine and/or non-human primate challenge models. In the current study, we evaluated neutralizing antibody responses using a pseudovirus with spike protein from the original SARS-CoV-2 strain. Several studies have demonstrated that SARS-CoV-2 pseudovirus neutralization assays are highly correlated with authentic virus neutralization assays and offer a reliable tool to compare different vaccination groups (Cantoni et al., 2021; Chmielewska et al., 2021). Though this plug-and-play platform is likely to induce similar immune

responses against other protein antigens, including those of other pathogens or SARS-CoV-2 variants, it will be important to directly evaluate neutralization and protective capacity of MAP-based vaccines against specific SARS-CoV-2 variants and other potential emerging pathogens.

## STAR★METHODS

Detailed methods are provided in the online version of this paper and include the following:

- **KEY RESOURCES TABLE**
- **RESOURCE AVAILABILITY**
  - Lead contact
  - Materials availability
  - Data and code availability
- **EXPERIMENTAL MODEL AND SUBJECT DETAILS**
  - Animals
  - HEK-293T-hACE2 cells
  - Human tissue samples
- **METHOD DETAILS**
  - Fabrication of dissolvable MAPs
  - Quantitation of MAP vaccine loading and delivery to skin
  - Skin immunofluorescence
  - Immunization of mice
  - Evaluation of SARS-CoV-2 specific antibody responses
  - SARS-CoV-2 pseudovirus neutralization assay
  - Systemic cytokine response to Poly(I:C) adjuvant
  - Evaluation of SARS-CoV-2 specific T cell responses
  - Human skin explants
- **QUANTIFICATION AND STATISTICAL ANALYSIS**

## SUPPLEMENTAL INFORMATION

Supplemental information can be found online at <https://doi.org/10.1016/j.isci.2022.105045>.

## ACKNOWLEDGMENTS

E.K. and L.D.F. are supported by NIH grants (UM1-AI106701, R01-AR079233, P50-CA254865 and UPMC Enterprises (IPA25565)). L.D.F. is also supported by NIH Grants (R01-AR074285 and R01-AR071277). E.K. and T.L.S. are supported by a grant from the Institute for Infection, Inflammation, and Immunity in Children (i4Kids). The graphical abstract and [Figure 1A](#) were created with [BioRender.com](https://BioRender.com). The authors also acknowledge the Petersen Institute of Nanoscience and Engineering at the University of Pittsburgh Swanson School of Engineering. This project used the UPMC Hillman Cancer Center and Tissue and Research Pathology/Pitt Biospecimen Core shared resource, which is supported in part by award P30-CA047904.

## AUTHOR CONTRIBUTIONS

Conceptualization, S.C.B., Z.G.G., E.K., and L.D.F.; Methodology, S.C.B., Z.G.G., C.D.C., G.E., and T.L.S.; Formal Analysis, S.C.B. and Z.G.G.; Investigation, S.C.B., Z.G.G., C.D.C., L.H.W., J.Z., P.S., M.A., T.L.S., and G.E.; Writing – Original Draft, S.C.B. and Z.G.G.; Writing – Review & Editing, S.C.B., Z.G.G., C.D.C., T.L.S., G.E., E.K., and L.D.F.; Visualization, S.C.B., Z.G.G., and M.A.; Supervision, E.K. and L.D.F.; Funding Acquisition, E.K. and L.D.F.

## DECLARATION OF INTERESTS

E. Korkmaz and L.D. Faló Jr. are inventors of related intellectual property. L.D. Faló Jr. is a co-founder and scientific advisor of SkinJect, a company that is developing dissolvable MAPs for treatment of non-melanoma skin cancer.

## INCLUSION AND DIVERSITY

We support inclusive, diverse, and equitable conduct of research.

Received: October 2, 2021  
Revised: April 19, 2022  
Accepted: August 25, 2022  
Published: October 21, 2022

## REFERENCES

- Al-Zahrani, S., Zaric, M., McCrudden, C., Scott, C., Kissenpennig, A., and Donnelly, R.F. (2012). Microneedle-mediated vaccine delivery: Harnessing cutaneous immunobiology to improve efficacy. *Expert Opin. Drug Deliv.* 9, 541–550. <https://doi.org/10.1517/17425247.2012.676038>.
- Arya, J., and Prausnitz, M.R. (2016). Microneedle patches for vaccination in developing countries. *J. Control. Release* 240, 135–141. <https://doi.org/10.1016/j.jconrel.2015.11.019>.
- Balmert, S.C., Carey, C.D., Faló, G.D., Sethi, S.K., Erdos, G., Korkmaz, E., and Faló, L.D. (2020). Dissolving undercut microneedle arrays for multicomponent cutaneous vaccination. *J. Control. Release* 317, 336–346. <https://doi.org/10.1016/j.jconrel.2019.11.023>.
- Bandyopadhyay, M., Morelli, A.E., Balmert, S.C., Ward, N.L., Erdos, G., Sumpter, T.L., Korkmaz, E., Kaplan, D.H., Oberbarnscheidt, M.H., and Tkacheva, O. (2022). Skin co-delivery of contact sensitizers and neurokinin-1 receptor antagonists integrated in microneedle arrays suppresses allergic contact dermatitis. *J. Allergy Clin. Immunol.* 150, 114–130. <https://doi.org/10.1016/j.jaci.2021.12.794>.
- Bardel, E., Doucet-Ladeveze, R., Mathieu, C., Harandi, A.M., Dubois, B., and Kaiserlian, D. (2016). Intradermal immunisation using the TLR3-ligand Poly (I:C) as adjuvant induces mucosal antibody responses and protects against genital HSV-2 infection. *NPJ Vaccines* 1, 16010. <https://doi.org/10.1038/npjvaccines.2016.10>.
- Benton, D.J., Wrobel, A.G., Xu, P., Roustan, C., Martin, S.R., Rosenthal, P.B., Skehel, J.J., and Gamblin, S.J. (2020). Receptor binding and priming of the spike protein of SARS-CoV-2 for membrane fusion. *Nature* 588, 327–330. <https://doi.org/10.1038/s41586-020-2772-0>.
- Bernard, J.J., Cowing-Zitron, C., Nakatsuji, T., Muehleisen, B., Muto, J., Borkowski, A.W., Martinez, L., Greidinger, E.L., Yu, B.D., and Gallo, R.L. (2012). Ultraviolet radiation damages self noncoding RNA and is detected by TLR3. *Nat. Med.* 18, 1286–1290. <https://doi.org/10.1038/nm.2861>.
- Boks, M.A., Bruijns, S.C., Ambrosini, M., Kalay, H., Van Bloois, L., Storm, G., De Grujil, T., and Van Kooyk, Y. (2015). In situ delivery of tumor antigen- and adjuvant-loaded liposomes boosts antigen-specific T-cell responses by human dermal dendritic cells. *J. Invest. Dermatol.* 135, 2697–2704. <https://doi.org/10.1038/jid.2015.226>.
- Borkowski, A.W., Park, K., Uchida, Y., and Gallo, R.L. (2013). Activation of TLR3 in keratinocytes increases expression of genes involved in formation of the epidermis, lipid accumulation, and epidermal organelles. *J. Invest. Dermatol.* 133, 2031–2040. <https://doi.org/10.1038/jid.2013.39>.
- Buglione-Corbett, R., Pouliot, K., Marty-Roix, R., West, K., Wang, S., Lien, E., and Lu, S. (2013). Serum cytokine profiles associated with specific adjuvants used in a DNA prime-protein boost vaccination strategy. *PLoS One* 8, e74820. <https://doi.org/10.1371/journal.pone.0074820>.
- Burny, W., Marchant, A., Hervé, C., Callegaro, A., Caubet, M., Fissette, L., Gheyle, L., Legrand, C., Ndour, C., and Da Silva, F.T. (2019). Inflammatory parameters associated with systemic reactivity following vaccination with adjuvanted hepatitis B vaccines in humans. *Vaccine* 37, 2004–2015. <https://doi.org/10.1016/j.vaccine.2019.02.015>.
- Callaway, E. (2021). COVID vaccine boosters: the most important questions. *Nature* 596, 178–180. <https://doi.org/10.1038/d41586-021-02158-6>.
- Cantoni, D., Mayora-Neto, M., and Temperton, N. (2021). The role of pseudotype neutralization assays in understanding SARS CoV-2. *Oxf. Open Immunol* 2, iqab005. <https://doi.org/10.1093/oximm/iqab005>.
- Channappanavar, R., Fett, C., Zhao, J., Meyerholz, D.K., and Perlman, S. (2014). Virus-specific memory CD8 T cells provide substantial protection from lethal severe acute respiratory syndrome coronavirus infection. *J. Virol.* 88, 11034–11044. <https://doi.org/10.1128/JVI.01505-14>.
- Chen, X., Fernando, G.J., Crichton, M.L., Flaim, C., Yukiko, S.R., Fairmaid, E.J., Corbett, H.J., Primiero, C.A., Ansaldo, A.B., Frazer, I.H., et al. (2011). Improving the reach of vaccines to low-resource regions, with a needle-free vaccine delivery device and long-term thermostabilization. *J. Control. Release* 152, 349–355. <https://doi.org/10.1016/j.jconrel.2011.02.026>.
- Chmielewska, A.M., Czarnota, A., Biełkowska-Szewczyk, K., and Grzyb, K. (2021). Immune response against SARS-CoV-2 variants: the role of neutralization assays. *NPJ Vaccines* 6, 142. <https://doi.org/10.1038/s41541-021-00404-6>.
- Chmielewska, A.M., Naddeo, M., Capone, S., Ammendola, V., Hu, K., Meredith, L., Verhoye, L., Rychłowska, M., Rappuoli, R., Ulmer, J.B., et al. (2014). Combined adenovirus vector and hepatitis C virus envelope protein prime-boost regimen elicits T cell and neutralizing antibody immune responses. *J. Virol.* 88, 5502–5510. <https://doi.org/10.1128/JVI.03574-13>.
- Chung, J.Y., Thone, M.N., and Kwon, Y.J. (2020). COVID-19 vaccines: the status and perspectives in delivery points of view. *Adv. Drug Deliv. Rev.* 170, 1–25. <https://doi.org/10.1016/j.addr.2020.12.011>.
- Connors, M., Graham, B.S., Lane, H.C., and Fauci, A.S. (2021). SARS-CoV-2 vaccines: much accomplished, much to learn. *Ann. Intern. Med.* 174, 687–691. <https://doi.org/10.7326/M21-0111>.
- Cunningham, C., Campion, S., Teeling, J., Felton, L., and Perry, V.H. (2007). The sickness behaviour and CNS inflammatory mediator profile induced by systemic challenge of mice with synthetic double-stranded RNA (poly I:C). *Brain Behav. Immun.* 21, 490–502. <https://doi.org/10.1016/j.bbi.2006.12.007>.
- De Clercq, E., Stewart, W.E., and de Somer, P. (1972). Interferon production linked to toxicity of polyribonucleoside acid-polyribocytidylic acid. *Infect. Immun.* 6, 344–347. <https://doi.org/10.1128/iai.6.3.344-347.1972>.
- Dioszeghy, V., Mondoulet, L., Puteaux, E., Dhelft, V., Ligouis, M., Plaqueot, C., Dupont, C., and Benhamou, P.-H. (2017). Differences in phenotype, homing properties and suppressive activities of regulatory T cells induced by epicutaneous, oral or sublingual immunotherapy in mice sensitized to peanut. *Cell. Mol. Immunol.* 14, 770–782. <https://doi.org/10.1038/cmi.2016.14>.
- Duan, L., Zheng, Q., Zhang, H., Niu, Y., Lou, Y., and Wang, H. (2020). The SARS-CoV-2 spike glycoprotein biosynthesis, structure, function, and antigenicity: implications for the design of spike-based vaccine immunogens. *Front. Immunol.* 11, 576622. <https://doi.org/10.3389/fimmu.2020.576622>.
- Erdos, G., Balmert, S.C., Carey, C.D., Faló, G.D., Patel, N.A., Zhang, J., Gambotto, A., Korkmaz, E., and Faló, L.D. (2020). Improved cutaneous genetic immunization by microneedle array delivery of an adjuvanted adenovirus vaccine. *J. Invest. Dermatol.* 140, 2528–2531. <https://doi.org/10.1016/j.jid.2020.03.966>.
- Fauci, A.S., Lane, H.C., and Redfield, R.R. (2020). Covid-19—navigating the uncharted. *N. Engl. J. Med.* 382, 1268–1269. <https://doi.org/10.1056/NEJMe2002387>.
- Feikin, D.R., Higdon, M.M., Abu-Raddad, L.J., Andrews, N., Araos, R., Goldberg, Y., Groome, M.J., Huppert, A., O'Brien, K.L., Smith, P.G., et al. (2022). Duration of effectiveness of vaccines against SARS-CoV-2 infection and COVID-19 disease: results of a systematic review and meta-regression. *Lancet* 399, 924–944. [https://doi.org/10.1016/S0140-6736\(22\)00152-0](https://doi.org/10.1016/S0140-6736(22)00152-0).
- Foged, C. (2011). Subunit vaccines of the future: the need for safe, customized and optimized particulate delivery systems. *Ther. Deliv.* 2, 1057–1077. <https://doi.org/10.4155/tde.11.68>.
- Fontanet, A., Autran, B., Lina, B., Kieny, M.P., Karim, S.S.A., and Sridhar, D. (2021). SARS-CoV-2 variants and ending the COVID-19 pandemic. *Lancet* 397, 952–954. [https://doi.org/10.1016/S0140-6736\(21\)00370-6](https://doi.org/10.1016/S0140-6736(21)00370-6).
- Foulds, K.E., Wu, C.Y., and Seder, R.A. (2006). Th1 memory: implications for vaccine development. *Immunol. Rev.* 211, 58–66. <https://doi.org/10.1111/j.0105-2896.2006.00400.x>.
- Frederiksen, L.S.F., Zhang, Y., Foged, C., and Thakur, A. (2020). The long road toward COVID-19 herd immunity: vaccine platform technologies and mass immunization strategies. *Front.*

- Immunol. 11, 1817. <https://doi.org/10.3389/fimmu.2020.01817>.
- Gill, H.S., Kang, S.M., Quan, F.S., and Compans, R.W. (2014). Cutaneous immunization: an evolving paradigm in influenza vaccines. *Expert Opin. Drug Deliv.* 11, 615–627. <https://doi.org/10.1517/17425247.2014.885947>.
- Giudice, E.L., and Campbell, J.D. (2006). Needle-free vaccine delivery. *Adv. Drug Deliv. Rev.* 58, 68–89. <https://doi.org/10.1016/j.addr.2005.12.003>.
- Hafner, A.M., Corthésy, B., and Merkle, H.P. (2013). Particulate formulations for the delivery of poly (I:C) as vaccine adjuvant. *Adv. Drug Deliv. Rev.* 65, 1386–1399. <https://doi.org/10.1016/j.addr.2013.05.013>.
- Hansson, M., Nygren, P.Å., and Ståhl, S. (2000). Design and production of recombinant subunit vaccines. *Biotechnol. Appl. Biochem.* 32, 95–107. <https://doi.org/10.1042/ba20000034>.
- Hayashi, T., Momota, M., Kuroda, E., Kusakabe, T., Kobari, S., Makisaka, K., Ohno, Y., Suzuki, Y., Nakagawa, F., and Lee, M.S. (2018). DAMP-inducing adjuvant and PAMP adjuvants parallelly enhance protective type-2 and type-1 immune responses to influenza split vaccination. *Front. Immunol.* 9, 2619. <https://doi.org/10.3389/fimmu.2018.02619>.
- Hirobe, S., Azukizawa, H., Hanafusa, T., Matsuo, K., Quan, Y.S., Kamiyama, F., Katayama, I., Okada, N., and Nakagawa, S. (2015). Clinical study and stability assessment of a novel transcutaneous influenza vaccination using a dissolving microneedle patch. *Biomaterials* 57, 50–58. <https://doi.org/10.1016/j.biomaterials.2015.04.007>.
- Irvine, D.J., Aung, A., and Silva, M. (2020). Controlling timing and location in vaccines. *Adv. Drug Deliv. Rev.* 158, 91–115. <https://doi.org/10.1016/j.addr.2020.06.019>.
- Jung, S.Y., Kang, K.W., Lee, E.Y., Seo, D.W., Kim, H.L., Kim, H., Kwon, T., Park, H.L., Kim, H., and Lee, S.M. (2018). Heterologous prime–boost vaccination with adenoviral vector and protein nanoparticles induces both Th1 and Th2 responses against Middle East respiratory syndrome coronavirus. *Vaccine* 36, 3468–3476. <https://doi.org/10.1016/j.vaccine.2018.04.082>.
- Kadoki, M., Patil, A., Thais, C.C., Brooks, D.J., Pandey, S., Deep, D., Alvarez, D., von Andrian, U.H., Wagers, A.J., and Nakai, K. (2017). Organism-level analysis of vaccination reveals networks of protection across tissues. *Cell* 171, 398–413. <https://doi.org/10.1016/j.cell.2017.08.024>.
- Kersten, G., and Hirschberg, H. (2007). Needle-free vaccine delivery. *Expert Opin. Drug Deliv.* 4, 459–474. <https://doi.org/10.1517/17425247.4.5.459>.
- Kim, E., Erdos, G., Huang, S., Kenniston, T.W., Balmert, S.C., Carey, C.D., Raj, V.S., Epperly, M.W., Klimstra, W.B., and Haagmans, B.L. (2020). Microneedle array delivered recombinant coronavirus vaccines: immunogenicity and rapid translational development. *EBioMedicine* 55, 102743. <https://doi.org/10.1016/j.ebiom.2020.102743>.
- Kim, J.D., Kim, M., Yang, H., Lee, K., and Jung, H. (2013). Droplet-born air blowing: novel dissolving microneedle fabrication. *J. Control. Release* 170, 430–436. <https://doi.org/10.1016/j.jconrel.2013.05.026>.
- Korkmaz, E., Balmert, S.C., Carey, C.D., Erdos, G., and Faló, L.D. (2021a). Emerging skin-targeted drug delivery strategies to engineer immunity: a focus on infectious diseases. *Expert Opin. Drug Deliv.* 18, 151–167. <https://doi.org/10.1080/17425247.2021.1823964>.
- Korkmaz, E., Balmert, S.C., Sumpter, T.L., Carey, C.D., Erdos, G., and Faló, L.D. (2021b). Microarray patches enable the development of skin-targeted vaccines against COVID-19. *Adv. Drug Deliv. Rev.* 171, 164–186. <https://doi.org/10.1016/j.addr.2021.01.022>.
- Kuwentrai, C., Yu, J., Rong, L., Zhang, B.Z., Hu, Y.F., Gong, H.R., Dou, Y., Deng, J., Huang, J.D., and Xu, C. (2021). Intradermal delivery of receptor-binding domain of SARS-CoV-2 spike protein with dissolvable microneedles to induce humoral and cellular responses in mice. *Bioeng. Transl. Med.* 6, e10202. <https://doi.org/10.1002/btm2.10202>.
- Lai, Y., Di Nardo, A., Nakatsuji, T., Leichter, A., Yang, Y., Cogen, A.L., Wu, Z.R., Hooper, L.V., Schmidt, R.R., von Aulock, S., et al. (2009). Commensal bacteria regulate Toll-like receptor 3-dependent inflammation after skin injury. *Nat. Med.* 15, 1377–1382. <https://doi.org/10.1038/nm.2062>.
- Lai, Y., and Gallo, R.L. (2008). Toll-like receptors in skin infections and inflammatory diseases. *Infect. Disord.: Drug Targets* 8, 144–155. <https://doi.org/10.2174/1871526510808030144>.
- Larregina, A.T., and Faló, L.D. (2005). Changing paradigms in cutaneous immunology: adapting with dendritic cells. *J. Invest. Dermatol.* 124, 1–12. <https://doi.org/10.1111/j.1523-1747.2004.23554.x>.
- Larregina, A.T., Morelli, A.E., Spencer, L.A., Logar, A.J., Watkins, S.C., Thomson, A.W., and Faló, L.D. (2001). Dermal-resident CD14+ cells differentiate into Langerhans cells. *Nat. Immunol.* 2, 1151–1158. <https://doi.org/10.1038/ni731>.
- Lebre, M.C., Antons, J.C., Kalinski, P., Schuitemaker, J.H., Van Capel, T.M., Kapsenberg, M.L., and De Jong, E.C. (2003). Double-stranded RNA-exposed human keratinocytes promote Th1 responses by inducing a type-1 polarized phenotype in dendritic cells: role of keratinocyte-derived tumor necrosis factor  $\alpha$ , type I interferons, and interleukin-18. *J. Invest. Dermatol.* 120, 990–997. <https://doi.org/10.1046/j.1523-1747.2003.12245.x>.
- Li, F. (2016). Structure, function, and evolution of coronavirus spike proteins. *Annu. Rev. Virol.* 3, 237–261. <https://doi.org/10.1146/annurev-virology-110615-042301>.
- Liu, L., Zhong, Q., Tian, T., Dubin, K., Athale, S.K., and Kupper, T.S. (2010). Epidermal injury and infection during poxvirus immunization is crucial for the generation of highly protective T cell-mediated immunity. *Nat. Med.* 16, 224–227. <https://doi.org/10.1038/nm.2078>.
- Longhi, M.P., Trumpfheller, C., Idoyaga, J., Caskey, M., Matos, I., Kluger, C., Salazar, A.M., Colonna, M., and Steinman, R.M. (2009). Dendritic cells require a systemic type I interferon response to mature and induce CD4+ Th1 immunity with poly IC as adjuvant. *J. Exp. Med.* 206, 1589–1602. <https://doi.org/10.1084/jem.20090247>.
- Marshall, S., Sahn, L.J., and Moore, A.C. (2016). The success of microneedle-mediated vaccine delivery into skin. *Hum. Vaccines Immunother.* 12, 2975–2983. <https://doi.org/10.1080/21645515.2016.1171440>.
- Martins, K.A., Cooper, C.L., Stronsky, S.M., Norris, S.L., Kwilas, S.A., Steffens, J.T., Benko, J.G., van Tongeren, S.A., and Bavari, S. (2016). Adjuvant-enhanced CD4 T cell responses are critical to durable vaccine immunity. *EBioMedicine* 3, 67–78. <https://doi.org/10.1016/j.ebiom.2015.11.041>.
- Mathers, A.R., and Larregina, A.T. (2006). Professional antigen-presenting cells of the skin. *Immunol. Res.* 36, 127–136. <https://doi.org/10.1385/IR.36:1:127>.
- Matsumoto, M., and Seya, T. (2008). TLR3: interferon induction by double-stranded RNA including poly(I:C). *Adv. Drug Deliv. Rev.* 60, 805–812. <https://doi.org/10.1016/j.addr.2007.11.005>.
- McCrudden, M.T., Torriss, B.M., Al-Zahrani, S., McCrudden, C.M., Zaric, M., Scott, C.J., Kissenpfennig, A., McCarthy, H.O., and Donnelly, R.F. (2015). Laser-engineered dissolving microneedle arrays for protein delivery: potential for enhanced intradermal vaccination. *J. Pharm. Pharmacol.* 67, 409–425. <https://doi.org/10.1111/jphp.12248>.
- McKay, P.F., Cizmeci, D., Aldon, Y., Maertzdorf, J., Weiner, J., Kaufmann, S.H., Lewis, D.J., van den Berg, R.A., Del Giudice, G., and Shattock, R.J. (2019). Identification of potential biomarkers of vaccine inflammation in mice. *Elife* 8, e46149. <https://doi.org/10.7554/eLife.46149>.
- McMillan, C.L., Azuar, A., Choo, J.J., Modhiran, N., Amarilla, A.A., Isaacs, A., Honeyman, K.E., Cheung, S.T., Liang, B., and Wurm, M.J. (2022). Dermal delivery of a SARS-CoV-2 subunit vaccine induces immunogenicity against variants of concern. *Vaccines* 10, 578. <https://doi.org/10.3390/vaccines10040578>.
- McMillan, C.L., Choo, J.J., Idris, A., Supramaniam, A., Modhiran, N., Amarilla, A.A., Isaacs, A., Cheung, S.T., Liang, B., and Bielefeldt-Olmann, H. (2021). Complete protection by a single-dose skin patch-delivered SARS-CoV-2 spike vaccine. *Sci. Adv.* 7, eabj8065. <https://doi.org/10.1126/sciadv.abj8065>.
- Mian, M.F., Ahmed, A.N., Rad, M., Babaian, A., Bowdish, D., and Ashkar, A.A. (2013). Length of dsRNA (poly I:C) drives distinct innate immune responses, depending on the cell type. *J. Leukoc. Biol.* 94, 1025–1036. <https://doi.org/10.1189/jlb.0312125>.
- Modjarrad, K. (2016). MERS-CoV vaccine candidates in development: the current landscape. *Vaccine* 34, 2982–2987. <https://doi.org/10.1016/j.vaccine.2016.03.104>.
- Morelli, A.E., Rubin, J.P., Erdos, G., Tkacheva, O.A., Mathers, A.R., Zahorchak, A.F., Thomson, A.W., Faló, L.D., and Larregina, A.T. (2005). CD4+ T cell responses elicited by different subsets of human skin migratory dendritic cells. *J. Immunol.* 175, 7905–7915. <https://doi.org/10.4049/jimmunol.175.12.7905>.
- Morens, D.M., and Fauci, A.S. (2020). Emerging pandemic diseases: How we got to COVID-19. *Cell* 182, 1077–1092. <https://doi.org/10.1016/j.cell.2020.08.021>.

- Moyle, P.M., and Toth, I. (2013). Modern subunit vaccines: development, components, and research opportunities. *ChemMedChem* 8, 360–376. <https://doi.org/10.1002/cmdc.201200487>.
- Nguyen, T.T., Oh, Y., Kim, Y., Shin, Y., Baek, S.K., and Park, J.H. (2020). Progress in microneedle array patch (MAP) for vaccine delivery. *Hum. Vaccines Immunother.* 17, 1–12. <https://doi.org/10.1080/21645515.2020.1767997>.
- O'Hagan, D.T., and De Gregorio, E. (2009). The path to a successful vaccine adjuvant—the long and winding road. *Drug Discov. Today* 14, 541–551. <https://doi.org/10.1016/j.drudis.2009.02.009>.
- Oosterhoff, D., Heusinkveld, M., Loughheed, S.M., Kosten, I., Lindstedt, M., Bruijns, S.C., van Es, T., van Kooyk, Y., van der Burg, S.H., and de Grijl, T.D. (2013). Intradermal delivery of TLR agonists in a human explant skin model: preferential activation of migratory dendritic cells by polyribosinic-polyribocytidylic acid and peptidoglycans. *J. Immunol.* 190, 3338–3345. <https://doi.org/10.4049/jimmunol.1200598>.
- Pan, Y., Liu, L., Tian, T., Zhao, J., Park, C.O., Lofftus, S.Y., Stingley, C.A., Yan, Y., Mei, S., and Liu, X. (2021). Epicutaneous immunization with modified vaccinia Ankara viral vectors generates superior T cell immunity against a respiratory viral challenge. *NPJ Vaccines* 6, 1. <https://doi.org/10.1038/s41541-020-00265-5>.
- Park, S., Lee, Y., Kwon, Y.M., Lee, Y.T., Kim, K.H., Ko, E.J., Jung, J.H., Song, M., Graham, B., and Prausnitz, M.R. (2018). Vaccination by microneedle patch with inactivated respiratory syncytial virus and monophosphoryl lipid A enhances the protective efficacy and diminishes inflammatory disease after challenge. *PLoS One* 13, e0205071. <https://doi.org/10.1371/journal.pone.0205071>.
- Perrie, Y., Mohammed, A.R., Kirby, D.J., McNeil, S.E., and Bramwell, V.W. (2008). Vaccine adjuvant systems: enhancing the efficacy of sub-unit protein antigens. *Int. J. Pharm.* 364, 272–280. <https://doi.org/10.1016/j.ijpharm.2008.04.036>.
- Prausnitz, M.R. (2017). Engineering microneedle patches for vaccination and drug delivery to skin. *Annu. Rev. Chem. Biomol. Eng.* 8, 177–200. <https://doi.org/10.1146/annurev-chembioeng-060816-101514>.
- Rodgers, A.M., Cordeiro, A.S., and Donnelly, R.F. (2019). Technology update: dissolvable microneedle patches for vaccine delivery. *Med. Devices* 12, 379–398. <https://doi.org/10.2147/MDER.S198220>.
- Rouphael, N.G., Paine, M., Mosley, R., Henry, S., McAllister, D.V., Kalluri, H., Pewin, W., Frew, P.M., Yu, T., and Thornburg, N.J. (2017). The safety, immunogenicity, and acceptability of inactivated influenza vaccine delivered by microneedle patch (TIV-MNP 2015): a randomised, partly blinded, placebo-controlled, phase 1 trial. *Lancet* 390, 649–658. [https://doi.org/10.1016/S0140-6736\(17\)30575-5](https://doi.org/10.1016/S0140-6736(17)30575-5).
- Salem, M.L., Kadima, A.N., Cole, D.J., and Gillanders, W.E. (2005). Defining the antigen-specific T-cell response to vaccination and poly (I:C)/TLR3 signaling: evidence of enhanced primary and memory CD8 T-cell responses and antitumor immunity. *J. Immunother.* 28, 220–228. <https://doi.org/10.1097/01.cji.0000156828.75196.0d>.
- Schmidt, S.V., Nino-Castro, A.C., and Schultze, J.L. (2012). Regulatory dendritic cells: there is more than just immune activation. *Front. Immunol.* 3, 274. <https://doi.org/10.3389/fimmu.2012.00274>.
- Schneider, L.P., Schoonderwoerd, A.J., Moutaftis, M., Howard, R.F., Reed, S.G., de Jong, E.C., and Teunissen, M.B. (2012). Intradermally administered TLR4 agonist GLA-SE enhances the capacity of human skin DCs to activate T cells and promotes emigration of Langerhans cells. *Vaccine* 30, 4216–4224. <https://doi.org/10.1016/j.vaccine.2012.04.051>.
- Shah, S.A., Oakes, R.S., Kapnick, S.M., and Jewell, C.M. (2022). Mapping the mechanical and immunological profiles of polymeric microneedles to enable vaccine and immunotherapy applications. *Front. Immunol.* 13, 843355. <https://doi.org/10.3389/fimmu.2022.843355>.
- Shin, M.D., Shukla, S., Chung, Y.H., Beiss, V., Chan, S.K., Ortega-Rivera, O.A., Wirth, D.M., Chen, A., Sack, M., Pokorski, J.K., et al. (2020). COVID-19 vaccine development and a potential nanomaterial path forward. *Nat. Nanotechnol.* 15, 646–655. <https://doi.org/10.1038/s41565-020-0737-y>.
- Sternberg, A., and Naujokat, C. (2020). Structural features of coronavirus SARS-CoV-2 spike protein: targets for vaccination. *Life Sci.* 257, 118056. <https://doi.org/10.1016/j.ifs.2020.118056>.
- Suh, H., Shin, J., and Kim, Y.C. (2014). Microneedle patches for vaccine delivery. *Clin. Exp. Vaccine Res.* 3, 42–49. <https://doi.org/10.7774/cevr.2014.3.1.42>.
- Sullivan, S.P., Koutsonanos, D.G., del Pilar Martin, M., Lee, J.W., Zarnitsyn, V., Choi, S.O., Murthy, N., Compans, R.W., Skountzou, I., and Prausnitz, M.R. (2010). Dissolving polymer microneedle patches for influenza vaccination. *Nat. Med.* 16, 915–920. <https://doi.org/10.1038/nm.2182>.
- Talaat, K.R., Halsey, N.A., Cox, A.B., Coles, C.L., Durbin, A.P., Ramakrishnan, A., and Bream, J.H. (2018). Rapid changes in serum cytokines and chemokines in response to inactivated influenza vaccination. *Influenza Other Respir. Viruses* 12, 202–210. <https://doi.org/10.1111/irv.12509>.
- Tohyama, M., Dai, X., Sayama, K., Yamasaki, K., Shirakata, Y., Hanakawa, Y., Tokumaru, S., Yahata, Y., Yang, L., and Nagai, H. (2005). dsRNA-mediated innate immunity of epidermal keratinocytes. *Biochem. Biophys. Res. Commun.* 335, 505–511. <https://doi.org/10.1016/j.bbrc.2005.07.105>.
- Verdijk, R.M., Mutis, T., Esendam, B., Kamp, J., Melief, C.J., Brand, A., and Goulmy, E. (1999). Polyribosinic polyribocytidylic acid (poly (I:C)) induces stable maturation of functionally active human dendritic cells. *J. Immunol.* 163, 57–61. <https://www.jimmunol.org/content/163/1/57>.
- Vrdoljak, A. (2013). Review of recent literature on microneedle vaccine delivery technologies. *Vaccine Dev. Therapy* 3, 47–55. <https://doi.org/10.2147/VDT.S34682>.
- Wang, J., Shah, D., Chen, X., Anderson, R., and Wu, M.X. (2014). A micro-sterile inflammation array as an adjuvant for influenza vaccines. *Nat. Commun.* 5, 4447. <https://doi.org/10.1038/ncomms5447>.
- Wang, N., Shang, J., Jiang, S., and Du, L. (2020). Subunit vaccines against emerging pathogenic human coronaviruses. *Front. Microbiol.* 11, 298. <https://doi.org/10.3389/fmicb.2020.00298>.
- Wang, Y., Wang, L., Cao, H., and Liu, C. (2021). SARS-CoV-2 S1 is superior to the RBD as a COVID-19 subunit vaccine antigen. *J. Med. Virol.* 93, 892–898. <https://doi.org/10.1002/jmv.26320>.
- Watanabe, A., Tatematsu, M., Saeki, K., Shibata, S., Shime, H., Yoshimura, A., Obuse, C., Seya, T., and Matsumoto, M. (2011). Raftlin is involved in the nucleocapture complex to induce poly (I:C)-mediated TLR3 activation. *J. Biol. Chem.* 286, 10702–10711. <https://doi.org/10.1074/jbc.M110.185793>.
- Wørzner, K., Sheward, D.J., Schmidt, S.T., Hanke, L., Zimmermann, J., McInerney, G., Hedestam, G.B.K., Murrell, B., Christensen, D., and Pedersen, G.K. (2020). Adjuvanted SARS-CoV-2 spike protein elicits neutralizing antibodies and CD4 T cell responses after a single immunization in mice. *EBioMedicine* 63, 103197. <https://doi.org/10.1016/j.ebiom.2020.103197>.
- Xia, D., Jin, R., Byagathvalli, G., Yu, H., Ye, L., Lu, C.Y., Bhamla, M.S., Yang, C., and Prausnitz, M.R. (2021). An ultra-low-cost electroporator with microneedle electrodes (ePatch) for SARS-CoV-2 vaccination. *Proc. Natl. Acad. Sci. USA* 118, e2110817118. <https://doi.org/10.1073/pnas.2110817118>.
- Yalcintas, E.P., Ackerman, D.S., Korkmaz, E., Telmer, C.A., Jarvik, J.W., Campbell, P.G., Bruchez, M.P., and Ozdoganlar, O.B. (2020). Analysis of in vitro cytotoxicity of carbohydrate-based materials used for dissolvable microneedle arrays. *Pharm. Res. (N. Y.)* 37, 33. <https://doi.org/10.1007/s11095-019-2748-7>.
- Zaric, M., Becker, P.D., Hervouet, C., Kalcheva, P., Doszpoly, A., Blattman, N., O'Neill, L.A., Yus, B.I., Cocita, C., and Kwon, S.Y. (2019). Skin immunisation activates an innate lymphoid cell-monocyte axis regulating CD8<sup>+</sup> effector recruitment to mucosal tissues. *Nat. Commun.* 10, 2214. <https://doi.org/10.1038/s41467-019-09969-2>.
- Zens, K.D., Chen, J.K., and Farber, D.L. (2016). Vaccine-generated lung tissue-resident memory T cells provide heterosubtypic protection to influenza infection. *JCI Insight* 1, e85832. <https://doi.org/10.1172/jci.insight.85832>.

**STAR★METHODS**

**KEY RESOURCES TABLE**

REAGENT or RESOURCE	SOURCE	IDENTIFIER
<b>Antibodies</b>		
Anti-mouse CD4 (clone GK1.5) BUV395	BD Biosciences	Cat# 563790; RRID: AB_2738426
Anti-mouse CD4 (clone RM4-5) PE-Cy7	BioLegend	Cat# 100528; RRID: AB_312729
Anti-mouse CD8b (clone H35-17.2) BUV737	BD Biosciences	Cat# 741811; RRID: AB_2871149
Anti-mouse CD45 (clone 30-F11) BUV395	BD Biosciences	Cat# 564279; RRID: AB_2651134
Anti-mouse IFN- $\gamma$ (clone XMG1.2) BV421	BD Biosciences	Cat# 563376; RRID: AB_2738165
Anti-mouse TNF (clone MP6-XT22)	BD Biosciences	Cat# 557730; RRID: AB_396838
Alexa Fluor 647		
Anti-mouse IL-2 (clone JES6-5H4)	BD Biosciences	Cat# 557725; RRID: AB_396833
Alexa Fluor 488		
Anti-mouse IL-4 (clone 11B11) PE	BD Biosciences	Cat# 554435; RRID: AB_395391
Anti-mouse CD44 (clone IM7) V500	BD Biosciences	Cat# 560781; RRID: AB_1937328
Anti-mouse CD16/CD32 (clone 2.4G2), Purified (Mouse BD Fc Block)	BD Biosciences	Cat# 553142; RRID: AB_394656
Anti-mouse I-A/I-E (clone M5/114.15.2) Janelia Fluor 549	Novus Biologicals	Cat# NBP1-43312JF549; RRID: AB_2922999
Anti-human HLA-DR (clone L243) Janelia Fluor 549	Novus Biologicals	Cat# NB100-77855JF549; RRID: AB_2923000
Anti-human HLA-DR (clone L243) Alexa Fluor 488	BioLegend	Cat# 307620; RRID: AB_493175
Anti-human CD1a (clone HI149) BUV395	BD Biosciences	Cat# 565300; RRID: AB_2739168
Anti-human CD14 (clone M5E2) PE-Cy7	BioLegend	Cat# 561385; RRID: AB_10611732
Anti-human CD40 (clone 5C3) BV605	BioLegend	Cat# 334335; RRID: AB_2564243
Anti-human CD80 (clone L307.4) V450	BD Biosciences	Cat# 560444; RRID: AB_1645583
Anti-human CD83 (clone HB15e) BV605	BioLegend	Cat# 305335; RRID: AB_2687382
Anti-human CD86 (clone 2331) V450	BD Biosciences	Cat# 560359; RRID: AB_1645585
Human BD Fc Block (clone Fc1.3216)	BD Biosciences	Cat# 564220; RRID: AB_2728082
Goat Anti-mouse IgG (polyclonal), Biotin-SP	Jackson ImmunoResearch	Cat# 115-065-071; RRID: AB_2338564
Goat Anti-mouse IgG1 (polyclonal), Biotin-SP	Jackson ImmunoResearch	Cat# 115-065-205; RRID: AB_2338571
Goat Anti-mouse IgG2c (polyclonal), Biotin-SP	Jackson ImmunoResearch	Cat# 115-065-208; RRID: AB_2338574
Anti-SARS-CoV-2 S1 (clone MM43)	Sino Biological	Cat# 40591-MM43; RRID: AB_2857934
Anti-SARS-CoV-2 Spike RBD (clone MM57)	Sino Biological	Cat# 40592-MM57; RRID: AB_2857935
Anti-SARS-CoV-2 Spike RBD (clone D006, chimeric)	Sino Biological	Cat# 40150-D006; RRID: AB_2827985
Goat anti-mouse IgG (polyclonal) HRP	Bio-Rad	Cat# 170-6516; RRID: AB_11125547
<b>Bacterial and virus strains</b>		
Replication-deficient murine leukemia virus (MLV) pseudotyped with SARS-CoV-2 spike protein (GenBank QHD43416.1) with firefly luciferase ORF	MyBioSource	Cat# MBS434275

(Continued on next page)

**Continued**

REAGENT or RESOURCE	SOURCE	IDENTIFIER
<b>Biological samples</b>		
Human skin tissue, healthy donor	Pitt Biospecimen Core <a href="http://www.pittbiospecimencore.pitt.edu/">http://www.pittbiospecimencore.pitt.edu/</a>	N/A
<b>Chemicals, peptides, and recombinant proteins</b>		
SARS-CoV-2 Spike S1 protein	Sino Biological	Cat# 40591-V08H
SARS-CoV-2 Spike RBD protein	Sino Biological	Cat# 40592-VNAH
Streptavidin HRP	BD Biosciences	Cat# 554066; RRID: AB_2868972
Polyinosinic-polycytidylic acid sodium salt (Poly(I:C))	Sigma-Aldrich	Cat# P1530; CAS# 42424-50-0
Carboxymethylcellulose sodium salt	Sigma-Aldrich	Cat# C5678; CAS# 9004-32-4
3,3',5,5-tetramethylbenzidine (TMB) peroxidase substrate	Sigma-Aldrich	Cat# T0440-1L; CAS# 64285-73-0
Polybrene infection / transfection reagent	Sigma-Aldrich	Cat# TR-1003
eBioscience Protein Transport Inhibitor Cocktail (500X)	ThermoFisher	Cat# 00-4980-03
eBioscience Cell Stimulation Cocktail (plus protein transport inhibitors) (500X)	ThermoFisher	Cat# 00-4975-93
SARS-CoV-2 Prot_S1 PepTivator	Miltenyi Biotec	Cat# 130-127-041
eBioscience Fixable Viability Dye eFluor 780	ThermoFisher	Cat# 65-0865-18
Stabilizing Fixative 3X Concentrate	BD Biosciences	Cat# 338036
SYLGARD 184 Silicone Elastomer Kit	Dow Corning	Cat# 04019862
Alexa Fluor 488 NHS Ester	ThermoFisher	Cat# A20000
Alexa Fluor 647 NHS Ester	ThermoFisher	Cat# A20006
SYBR Green I Nucleic Acid Stain	ThermoFisher	Cat# S7563
DAPI	ThermoFisher	Cat# D1306; CAS# 28718-90-3
Brilliant Stain Buffer Plus	BD Biosciences	Cat# 566385
FIX & PERM Cell Permeabilization Kit	ThermoFisher	Cat# GAS004
autoMACS Running Buffer	Miltenyi Biotec	Cat# 130-091-221
Normal Goat Serum	Jackson ImmunoResearch	Cat# 005-000-121; RRID: AB_2336990
BSA (IgG- and protease-free)	Jackson ImmunoResearch	Cat# 001-000-162; RRID: AB_2336946
<b>Critical commercial assays</b>		
Mouse IFN-beta DuoSet ELISA	R&D Systems	Cat# DY8234-05
Mouse IL-6 DuoSet ELISA	R&D Systems	Cat# DY406-05
Mouse CCL5/RANTES DuoSet ELISA	R&D Systems	Cat# DY478-05
Mouse IFN-gamma DuoSet ELISA	R&D Systems	Cat# DY485-05
Mouse TNF-alpha DuoSet ELISA	R&D Systems	Cat# DY410-05
ONE-Glo Luciferase Assay System	Promega	Cat# E6110
<b>Experimental models: Cell lines</b>		
HEK-293T-hACE2	BEI Resources	Cat# NR-52511; RRID: CVCL_A7UK
<b>Experimental models: Organisms/strains</b>		
Mouse: C57BL/6J	Jackson Laboratory	Strain #000664; RRID: IMSR_JAX:000664
<b>Software and algorithms</b>		
FlowJo software v10	FlowJo, LLC	RRID: SCR_008520; <a href="https://www.flowjo.com/">https://www.flowjo.com/</a>
GraphPad Prism 9	GraphPad Software, LLC	RRID: SCR_002798; <a href="https://www.graphpad.com/scientific-software/prism/">https://www.graphpad.com/scientific-software/prism/</a>

(Continued on next page)

**Continued**

REAGENT or RESOURCE	SOURCE	IDENTIFIER
Living Image 4.3	PerkinElmer	RRID: SCR_014247; <a href="https://www.perkinelmer.com/lab-products-and-services/resources/in-vivo-imaging-software-downloads.html">https://www.perkinelmer.com/lab-products-and-services/resources/in-vivo-imaging-software-downloads.html</a>
ImageJ 1.53c	NIH	RRID: SCR_003070; <a href="https://imagej.nih.gov/ij/">https://imagej.nih.gov/ij/</a>

## RESOURCE AVAILABILITY

### Lead contact

Further information and requests for resources and reagents should be directed to and will be fulfilled by the lead contact, Louis D. Faló Jr. ([lof2@pitt.edu](mailto:lof2@pitt.edu)).

### Materials availability

This study did not generate new unique reagents.

### Data and code availability

All data reported in this paper will be shared by the [lead contact](#) upon reasonable request. This paper does not report original code. Any additional information required to reanalyze the data reported in this paper is available from the [lead contact](#) upon request.

## EXPERIMENTAL MODEL AND SUBJECT DETAILS

### Animals

Female C57BL/6 mice were purchased from The Jackson Laboratory (Bar Harbor, ME) and used at 6-8 weeks of age. Mice were maintained under specific pathogen-free conditions at the University of Pittsburgh, and experiments were conducted in accordance with Institutional Animal Care and Use Committee (IACUC) guidelines. Numbers of mice used for each experiment are noted in the corresponding figure legends.

### HEK-293T-hACE2 cells

Human embryonic kidney cells expressing human angiotensin-converting enzyme 2 (HEK-293T-hACE2, female, #NR-52511) were obtained through BEI Resources, NIAID, NIH, and were maintained in DMEM media (HyClone #SH30243.01) supplemented with 10% fetal bovine serum (FBS, R&D Systems #S11550H) and penicillin-streptomycin (100 IU/mL, 100 µg/mL; Gibco).

### Human tissue samples

Discarded normal skin was obtained through our institutional tissue bank with informed consent from three healthy female donors (ages 20-29, 40-49, and 50-55 years) undergoing surgical procedures at the University of Pittsburgh Medical Center (UPMC). The de-identified tissue specimens were acquired through the Pitt Biospecimen Core with institutional review board approval (IRB #0501119).

## METHOD DETAILS

### Fabrication of dissolvable MAPs

Dissolvable MAPs integrating vaccine components, recombinant SARS-CoV-2 S1 spike protein (#40591-V08H, Sino Biological, Beijing, China) ± polyinosinic-polycytidylic acid sodium salt (Poly(I:C)) (#P1530, Sigma-Aldrich, St. Louis, MO), were fabricated using our published manufacturing strategy ([Balmert et al., 2020](#)). High-quality master MAPs, which consist of hundred obelisk-shaped micro-scale projections with the projection length and width of 750 and 225 µm, respectively, in a 10 × 10 array, were manufactured using two-photon polymerization 3D printing (Nanoscribe Photonic Professional, GT; Nanoscribe GmbH & Co. KG, Germany). To facilitate skin penetration without mechanical failure, these obelisk-shaped microprotrusions included filleted bases and were spaced in the array with a tip-to-tip distance of 675 µm. To show the quality of 3D-printed microprotrusions, master MAPs were imaged by optical stereomicroscopy. Importantly, we have successfully utilized the same MAP design in ongoing phase I clinical trials ([ClinicalTrials.gov](https://clinicaltrials.gov/ct2/show/study/NCT02192021) Identifier: NCT02192021). Next, micromolding steps, enabled by master MAPs, were employed to create MAP production molds from an elastomer, polydimethylsiloxane (PDMS: SYLGARD

184 from Dow Corning, Midland, MI; 10:1 base material to curing agent ratio), resulting in flexible molds with obelisk-shaped wells. Vaccine-loaded MAPs were then produced from carboxymethylcellulose sodium salt (CMC, 90 kDa MW; #C5678, Sigma-Aldrich) by spin-casting of vaccine components (S1 ± Poly(I:C)) and CMC into the wells of MAP production molds in a sequential fashion with centrifugation at room temperature. Casting of S1 antigen and Poly(I:C) adjuvant was performed by (1) loading 20 μL of solution of 8.33 mg S1 ± 41.67 mg Poly(I:C) per mL into each MAP reservoir on the PDMS production molds, (2) centrifuging for 1 min at 4500 rpm to fill the wells of MAP production molds, (3) recovering excess biocargo solution within the reservoir, and (4) centrifuging for 30 min at 4500 rpm to dry biocargo in the production molds. After loading vaccine components, CMC hydrogel, prepared in endotoxin-free water (HyClone Cell Culture Grade Water) at a total solute concentration of 20% w/w, was loaded onto each MAP in the PDMS production molds (50 μL each) to form the final vaccine loaded MAPs. Hydrogel-loaded PDMS molds were centrifuged (3 h at 4500 rpm) to obtain the final dissolvable MAPs for cutaneous vaccination experiments. Fabricated MAPs were imaged using optical stereomicroscopy (ZEISS Stemi, 2000-C microscope with Olympus OM-D E-M5 II camera) to assess the geometric integrity of the micron-scale sharp protrusions. To evaluate dissolution kinetics in mouse abdominal skin and human skin explants, MAPs were also imaged using a FEI Apreo scanning electron microscope (ThermoFisher) before and after application for 5, 10, or 15 min. Blank MAPs without any biocargo were prepared from CMC for control experiments with human skin explants. In addition, S1 and Poly(I:C) were labeled using Alexa Fluor 488 (A20000, ThermoFisher) and Alexa Fluor 647 (A20006, ThermoFisher) fluorescent dyes, respectively, and S1 AF488 + Poly(I:C) AF647 MAPs were fabricated for visualization of MAP-mediated cutaneous delivery of the multicomponent COVID-19 vaccine.

### Quantitation of MAP vaccine loading and delivery to skin

The amount of S1 and Poly(I:C) integrated in MAPs was determined by dissolving MAPs overnight in RNase-free Ambion TE Buffer (pH = 8), followed by S1-specific sandwich ELISA, or SYBR Green nucleic acid detection reagent (Invitrogen), respectively. The following antibodies were used for the ELISA: Sino Biological #40150-D006 capture antibody (1:5000), Sino Biological #40591-MM43 detection antibody (1 μg/mL), and HRP-conjugated goat anti-mouse IgG secondary from BioRad #170-6516 (1:3000).

MAP-mediated delivery of multicomponent COVID-19 vaccine into C57BL/6 mouse skin *in vivo* or freshly excised human skin explants was evaluated using an IVIS imaging system. S1 AF488 + Poly(I:C) AF647 MAPs were fabricated as described above, manually applied to the abdomen of anesthetized mice for 15 min *in vivo*, or to freshly excised human skin samples for 5 min, and then removed using tweezers. The MAP-treated murine and human skin samples were imaged with a live animal fluorescence *in vivo* imaging system (IVIS Lumina XR, PerkinElmer, Waltham, MA) to detect S1 AF488 and Poly(I:C) AF647 at the MAP application sites. Images were post-processed using Living Image software (PerkinElmer). Delivery of S1 and Poly(I:C) from MAPs was also quantified by dissolving MAPs in water and comparing fluorescence signal before and after skin applications using a SpectraMax iD5 Hybrid Multi-Mode Microplate reader (Molecular Devices, San Jose, CA). Application sites in mice and human skin were then prepared for skin immunofluorescence analysis.

### Skin immunofluorescence

After the application of S1 AF488 + Poly(I:C) AF647 MAPs, the skin was flash-frozen in optimal cutting temperature (OCT) compound and cryosectioned (9 μm thick). Sections were fixed with 96% ethanol, blocked with PBS containing 5% donkey serum, incubated with Janelia Fluor 549-labeled antibodies for MHC class II mouse I-A/I-E (M5/114.15.2) or human HLA-DR (L243); Novus Biologicals, Centennial, CO, counterstained with DAPI, and fixed with 2% paraformaldehyde. Slides were imaged with a Keyence BZ-X800 fluorescence microscope (Osaka, Japan), and channels were merged using ImageJ software.

### Immunization of mice

Mice were immunized and boosted similarly 14 days later by application of 20 μg recombinant SARS-CoV-2 S1 protein ± 100 μg Poly(I:C) MAP to shaved abdominal skin or by intramuscular (IM) injection of S1 protein (20 μg in 20 μL sterile PBS) into the hindlimb gastrocnemius muscle. Naive mice served as controls. For T cell assays, mice were euthanized 5 days after boosting (day 19), or 5 weeks after boosting (day 50). For serum antibody measurements, blood samples were taken via saphenous vein 2, 4, 6, 20, 36, 44, 58, and 77 weeks after primary immunization, and serum was isolated by centrifugation.

### Evaluation of SARS-CoV-2 specific antibody responses

SARS-CoV-2 S1- or RBD-specific binding antibodies in serum, lung homogenates, and/or bronchoalveolar lavage (BAL) fluid were measured by indirect ELISAs. Serum was collected at the time points describe above. Some mice were euthanized six weeks after primary immunization, and BAL fluid (1 mL PBS per mouse) was collected. Both lungs from each mouse were then isolated and homogenized in 1 mL PBS using a Bullet Blender Storm 24 and Navy RINO tubes pre-filled with stainless steel beads (Next Advance, Averill Park, NY). Lung tissue homogenates were centrifuged for 5 min at 1000xg, and supernatants were saved for anti-S1 IgG measurement by ELISA. For ELISAs, Costar EIA/RIA plates (Corning Inc., Corning, NY) were coated with 100  $\mu$ L/well of 1  $\mu$ g/mL recombinant SARS-CoV-2 S1 spike protein (Sino Biological #40591-V08H) or spike RBD protein (Sino Biological #40592-VNAH) in PBS by overnight incubation at 4°C. Plates were washed three times with 0.05% Tween 20 in PBS and blocked with 1% normal goat serum (Jackson ImmunoResearch, West Grove, PA) in PBS for 1 h at 37°C. Serum samples and standard antibodies were diluted in blocking buffer, added to plates, and incubated for 2 h at 37°C. After washing (3x), plates were incubated for 1 h at 37°C with biotinylated secondary antibodies (goat anti-mouse IgG, IgG1, or IgG2c; Jackson ImmunoResearch), diluted 1:20,000 in blocking buffer. Plates were then washed (3x) and incubated for 30 min at 37°C with streptavidin-HRP (BD Biosciences), diluted 1:1000 in blocking buffer. After a final wash (3x), plates were developed with 3,3',5,5'-tetramethylbenzidine (TMB) peroxidase substrate (Sigma-Aldrich) for 2 min at room temperature, and the reaction was quenched with 1 M H<sub>2</sub>SO<sub>4</sub>. For all ELISAs, optical density at 450 nm (OD450) was read with a SpectraMax Hybrid Multi-Mode Microplate Reader. Antigen-specific total IgG concentrations in serum, BAL fluid, or lung homogenates were calculated from standard curves generated with S1-specific monoclonal mouse IgG1, or RBD-specific monoclonal mouse IgG2b antibodies (Sino Biological #40591-MM43 or #40592-MM57, respectively). For S1-specific IgG1 and IgG2c titers, three-fold serial dilutions of serum were used, and a control sample was included on each plate to allow normalization of OD450 values between plates. Endpoint titers were calculated as reciprocals of maximum dilutions for which OD450 values exceeded the mean plus three standard deviations of OD450 values for naïve serum.

### SARS-CoV-2 pseudovirus neutralization assay

Replication-deficient murine leukemia virus (MLV) pseudotyped with the SARS-CoV-2 spike protein (GenBank QHD43416.1) and containing a firefly luciferase ORF as a reporter was obtained from MyBioSource (#MBS434275). For neutralization assays, HEK-293T-hACE2 cells were plated at a density of  $1.5 \times 10^4$  cells/well in 50  $\mu$ L media in 96-well, white, clear bottom, poly-D-lysine coated plates (Thermo Scientific Nunc #152028) and incubated overnight at 37°C with 5% CO<sub>2</sub>. Serum samples were heat-inactivated at 56°C for 30 min and then diluted in media in 96-well round-bottom plates (Corning Costar #3799). After adding 55  $\mu$ L pseudovirus to 20  $\mu$ L diluted serum, two-fold serial dilutions of serum ranged from 1:5 to 1:160. Serial dilutions of anti-S1 neutralizing antibody (Sino Biological #40591-MM43) were used to validate the assay. Diluted serum, or neutralizing antibodies, were incubated with SARS-CoV-2 pseudovirus for 1 h at 37°C, and then 70  $\mu$ L/well transferred to cells. Polybrene (Sigma #TR-1003) was added with a final concentration of 5  $\mu$ g/mL and a final volume of 150  $\mu$ L per well. Cells were incubated at 37°C with 5% CO<sub>2</sub> for 42 h, and then clear bottoms of plates covered with white backing tape (PerkinElmer #6005199). Luciferase activity was measured using a ONE-Glo Luciferase Assay System (Promega #E6110) and luminescence read on a SpectraMax iD5 Hybrid Multi-Mode Microplate Reader. After subtracting baseline luminescence from control wells without pseudovirus, the percent inhibition of pseudovirus infection was calculated by normalizing luminescence to that from control wells with pseudovirus. Half maximal inhibitory dilution (ID50) neutralizing titers were determined by nonlinear least-squares regression using an inhibitor vs. normalized response, variable slope model, where % Inhibition =  $100/(1+(ID50/Dilution)^{HillSlope})$ , with ID50 > 0 and HillSlope < 0 constraints, no weighting, and medium convergence criteria (GraphPad Prism v9).

### Systemic cytokine response to Poly(I:C) adjuvant

Female C57BL/6J mice were administered 100  $\mu$ g Poly(I:C) via intramuscular injection (in 20  $\mu$ L PBS) into the hindlimb gastrocnemius muscle, or via a MAP applied to the shaved abdominal skin. Intramuscular PBS and Blank MAPs served as vehicle controls. Blood samples were obtained from saphenous veins 3 and 6 h after treatment, and from terminal cardiac puncture under anesthesia at 12 h. Serum samples were diluted 1:10 in PBS with 1% BSA (BSA; IgG- and protease-free; Jackson ImmunoResearch), and concentrations of IFN- $\beta$ , IL-6, CCL5, TNF, and IFN- $\gamma$  were measured using the corresponding mouse DuoSet ELISA kits (R&D Systems, Minneapolis, MN).

### Evaluation of SARS-CoV-2 specific T cell responses

Splenocytes were isolated from naive or immunized mice and RBCs lysed. Lymphocytes were isolated from lungs, as previously described (Kadoki et al., 2017). Splenocytes ( $1.5 \times 10^6$ ) or lung resident lymphocytes ( $\sim 2\text{--}6 \times 10^5$ ) were stimulated in 96-well U-bottom plates (150  $\mu\text{L}$  per well) with SARS-CoV-2 Prot\_S1 PepTivator (0.6 nmol/mL or  $\sim 1 \mu\text{g/mL}$  each peptide; Miltenyi Biotec, Auburn, CA) diluted in RPMI 1640 media (Gibco, Gaithersburg, MD) supplemented with 10% fetal bovine serum (FBS; premium select, heat-inactivated; R&D Systems), 10 mM HEPES (Lonza, Walkersville, MD), 2 mM L-glutamine (Gibco), 1 mM sodium pyruvate (Sigma), 1X antibiotic-antimycotic solution (Sigma), 1X non-essential amino acids (NEAA; Lonza), and 55  $\mu\text{M}$  2-mercaptoethanol (Gibco). Cells were cultured for 6 h at 37°C, and 1X Protein Transport Inhibitor Cocktail (brefeldin A and monensin; eBioscience) was added for the last 4 h. For positive controls, cells were treated with 1X Cell Stimulation Cocktail plus Protein Transport Inhibitors (eBioscience), and unstimulated cells were used as negative controls. After stimulation, cells were incubated with Mouse BD Fc Block (2.4G2) and stained with antibodies for CD4 (GK1.5, BUV395, BD; or RM4-5, PE-Cy7, BioLegend), CD8b (H35-17.2, BUV737, BD), CD45 (30-F11, BUV395, BD), and a fixable viability dye (FVD, eFluor 780, eBioscience). For evaluation of memory T cell responses 5 weeks after boosting, cells were also stained with an antibody for CD44 (IM7, V500, BD). Fix & Perm Cell Permeabilization Kit (Invitrogen) was used for intracellular cytokine staining, along with antibodies for IFN- $\gamma$  (XMG1.2, BV421, BD), TNF (MP6-XT22, Alexa 647, BD), IL-2 (JES6-5H4, Alexa 488, BD), and IL-4 (11B11, PE, BD). Surface and intracellular staining were performed in the presence of Brilliant Stain Buffer Plus (BD). Stained cells were fixed with 1X BD Stabilizing Fixative, and flow cytometric analysis was performed using a BD LSR II flow cytometer (BD Biosciences) and FlowJo v10 software (FlowJo LLC, Ashland, OR). Multifunctional SARS-CoV-2 S1-specific T cells were identified by cytokine production and quantified using the Boolean gating function in FlowJo. The gating strategies used for analyses of T cells in spleens and lungs are presented in Figures S3 and S6, respectively. To account for non-specific activation, frequencies of cytokine positive cells from unstimulated controls were subtracted from corresponding peptide-stimulated samples, and negative values were set to zero.

### Human skin explants

After bulk fat removal from normal skin tissue samples, skin explants were harvested with a Silver's miniature skin graft knife (Padgett, Integra Miltex, Plainsboro, NJ). Explants were cut into 1  $\times$  2 cm rectangles, washed with 70% ethanol and twice with PBS, and placed epidermis up on sterile filter paper on a silicone backing. To address reproducibility issues inherent in human samples, a portion of each skin sample from each unique patient served as an internal negative (untreated) control and the experimental data were normalized with respect to that control. MAPs (2 per explant) were applied to human skin explants. After 5 min, MAPs were removed and explants placed epidermis up on steel mesh rafts (1 mm pores) in 6-well plates (Falcon, Corning) with AIM-V serum-free media (Gibco #12055-083) supplemented with 2.5  $\mu\text{g/mL}$  Amphotericin B (HyClone). This arrangement maintains an air-epidermal interface, while the dermis is in contact with media. After for 48 h culture at 37°C in 5% CO<sub>2</sub>, cells that migrated out of explants into the media were incubated with Human BD Fc Block and then stained with antibodies for HLA-DR (L243, Alexa 488, BioLegend), CD1a (HI149, BUV395, BD), CD14 (M5E2, PE-Cy7, BioLegend), CD40 (5C3, BV605, BioLegend), CD80 (L307.4, V450, BD), CD83 (HB15e, BV605, BioLegend), CD86 (2331, V450, BD), and a fixable viability dye (FVD, eFluor 780, eBioscience), in the presence of Brilliant Stain Buffer Plus (BD). Stained cells were fixed with 1X BD Stabilizing Fixative, and flow cytometric analysis was performed using a BD LSR II flow cytometer and FlowJo v10 software. The gating strategy is presented in Figure S10.

### QUANTIFICATION AND STATISTICAL ANALYSIS

All statistical analyses were performed using GraphPad Prism v9 (San Diego, CA), and specific statistical tests used for each experiment are described in the figure legends. Differences were considered significant if  $p < 0.05$ .